

# CHIRALITY VIOLATION IN QCD REGGEON INTERACTIONS\*

Alan. R. White<sup>†</sup>

High Energy Physics Division  
Argonne National Laboratory  
9700 South Cass, IL 60439, USA.

## Abstract

The appearance of the triangle graph infra-red axial anomaly in reduced quark loops contributing to QCD triple-regge interactions is studied. In a dispersion relation formalism, the anomaly can only be present in the contributions of unphysical triple discontinuities. In this paper an asymptotic discontinuity analysis is applied to high-order feynman diagrams to show that the anomaly does indeed occur in sufficiently high-order reggeized gluon interactions. The reggeon states involved must contain reggeized gluon combinations with the quantum numbers of the anomaly (winding-number) current. A direct connection with the well-known U(1) problem is thus established. Closely related diagrams that contribute to the pion/pomeron and triple pomeron couplings in color superconducting QCD are also discussed.

---

\*Work supported by the U.S. Department of Energy, Division of High Energy Physics, Contracts W-31-109-ENG-38 and DEFG05-86-ER-40272

<sup>†</sup>arw@hep.anl.gov

# 1. INTRODUCTION

It is commonly believed that non-perturbative quark chirality transitions play an important role within the QCD bound-state S-Matrix. Assuming that the theory can be quantized via a suitably defined euclidean path-integral<sup>‡</sup>, the chirality transitions are understood as originating from gauge-dependent non-perturbative classical solutions with non-trivial topology. Field configurations of this kind produce zero modes of the Dirac operator which[2] prevent the gauge-invariant separation of massless fermion fields into right- and left-handed components that separately create particles and antiparticles. The resulting violation of axial charge conservation is described by the anomalous divergence equation for the U(1) axial current. While many consequences of chirality violation are understood, for example the generation[3] of a mass for the  $\eta'$ , its full significance in determining the non-perturbative massless S-Matrix is far from understood. In particular, the role of chirality violation due to topological gauge fields in chiral symmetry breaking is the subject of much debate[4, 5].

In this paper, and a companion paper[6], we provide a completely different understanding of chirality transitions in the massless, high-energy, QCD bound-state S-Matrix. No mention is made of euclidean path-integral quantization or topological fields. Rather, as we explain further below, our arguments are based directly on the singularity structure of high-order feynman diagrams that contribute to the high-energy scattering of bound-states.

It is well established[7] that when the gauge symmetry of QCD is spontaneously broken general high-energy limits (multi-regge limits) of quark and gluon amplitudes are described perturbatively by reggeon diagrams in which the reggeons are simply massive, reggeized, gluons and quarks. Both  $t$ - and  $s$ - channel unitarity are satisfied. Reggeon interactions are described, in general, by “reduced” feynman diagrams, obtained from underlying diagrams by placing some propagators on-shell. It is important, however, to distinguish two kinds of interaction vertices. The simplest kind are those that describe the repeated interaction of reggeons “propagating” in a single reggeon channel (for which there is only one overall transverse momentum). The well-known BFKL kernel is, essentially, an example of this kind of vertex. The second kind are the vertices that couple different reggeon channels, the simplest being the triple-regge vertices[8] that couple three reggeon channels - each carrying a separate transverse momentum. In the massless theory such vertices should contain the couplings of bound-state reggeons (e.g. pions and nucleons) together with their couplings to the physical pomeron. Effectively, therefore, vertices of this kind determine the bound-states of the theory and their high-energy scattering amplitudes.

---

<sup>‡</sup>We note, though, that the elimination of unphysical degrees of freedom remains an unsolved problem[1].

There are, of course, no axial-vector currents in the QCD interaction but in the reduced diagrams providing the crucial triple-regge vertices, components of an axial-vector interaction can appear. Therefore, we have suggested[10] that, in sufficiently high orders, chirality violation due to the infra-red triangle anomaly should appear in reggeized gluon interactions of this kind. The purpose of this paper is to finally establish that this is the case. It is necessary, however, to study very high-order diagrams.

We have long believed[9] that the massless, bound-state, multi-regge, S-Matrix should be obtainable from the massive reggeon diagrams once the infra-red role of the chiral anomaly is determined. In previous papers we have outlined[11, 12] how (appropriately regularized) anomaly interactions can be the essential element that, in combination with the infra-red divergences of the massless limit, produce the “non-perturbative” properties of confinement and chiral symmetry breaking. We argued that, while the anomaly interactions cancel when the scattering states are perturbative quarks and gluons, for compound multiregge states with an appropriate infra-red component such interactions dominate and infra-red divergences self-consistently produce the bound-state S-Matrix. However, to demonstrate this via the construction of a full set of multi-regge amplitudes is a complicated project which, of necessity, will involve much abstract multi-regge theory. While this construction is still our eventual goal, as an intermediate step, we have first developed, in the companion paper to this, a calculational method that demonstrates the dynamical role of the anomaly while avoiding the (little known) multi-regge formalism as much as possible. Light-cone properties of the anomaly are heavily exploited and we are able to show how both the U(1) and chiral flavor anomaly play essential roles.

By studying the interaction of (infinite momentum) axial currents we show[6] that, when the SU(3) gauge symmetry is partially broken to SU(2), U(1) anomaly interactions combine with couplings due to the flavor anomaly to produce an infra-red divergent amplitude for the scattering of Goldstone boson “pions” and “nucleons”. The flavor anomaly produces the pion particle poles, while the U(1) anomaly produces the high-energy coupling of the pions to the exchanged pomeron. After the divergence is factorized off, as a wee gluon condensate within the scattering states, the remaining amplitudes have both confinement and chiral symmetry breaking. (The wee gluon condensate can be identified directly with the infra-red component of multi-regge states that appears in the multi-regge program.) It is apparent that the nature of the pomeron is crucially dependent on chiral symmetry breaking. We anticipate that restoration of full SU(3) gauge symmetry will result from randomization of the SU(2) condensate within SU(3) and that the Critical Pomeron[13] will appear.

The main focus of this paper will be on multigluon reggeon interactions that are most directly relevant to the general multi-regge program and the pomeron interactions that emerge. However, as we briefly describe at the end of this paper, the

multi-quark/gluon interaction that provides the pion/pomeron coupling in [6] is very closely related to the reggeized gluon interactions that we study. We will establish, remarkably perhaps, that for the anomaly to appear the reggeon states involved must contain gluon combinations with the quantum numbers of the anomaly (winding-number) current. The conventional U(1) problem is, therefore, clearly encountered. We will concentrate on isolating the anomaly via infra-red properties. Nevertheless, although we will discuss this only briefly at a few key points, we expect the infra-red phenomena we discuss to be connected to “ultra-violet” reggeon interaction problems (involving momenta flowing around an internal quark loop that are comparable in magnitude to large external momenta) where short-distance interactions of the winding number current appear directly. That the anomaly is a high-order, many gluon, phenomenon is not surprising if the anomaly current, containing a product of three gluon fields, has to be involved.

Properties of the triangle diagram are discussed in detail in the companion paper[6], where a complete set of the relevant references is given. For our present purposes we note that the massless axial-vector graph has an infra-red divergence that involves a zero four-momentum fermion propagator. Both the “particle” and “antiparticle” poles of this propagator contribute to the divergence. The coupling at one end of the propagator can be viewed as the vertex for production of the particle while simultaneously (and symmetrically) that at the other end describes the production of the antiparticle. If the zero momentum propagator describes a physical transition it implies that there is, necessarily, an accompanying “spectral flow” of the fermion energy spectrum so that the production of the antiparticle (or the particle) corresponds to the production of a Dirac hole state, i.e. the absorption of a particle (antiparticle). In this way, the transition is understood as a “chirality transition”

In Minkowski space the Dirac zero modes due to topological gauge fields do indeed produce[2] spectral flow (with time) of the eigenvalues of the corresponding (gauge-dependent) “Hamiltonian”. However, since there is no complete non-perturbative Hamiltonian formalism for massless QCD, there is no understanding of the full consequences of spectral flow<sup>§</sup>. The phenomenon we see is, arguably, the minimum spectral flow that could be present (if there is any). Zero momentum fermion states identified initially as a particle (within a boundstate) can evolve with time into a filled vacuum state of the corresponding Dirac sea and, similarly, filled vacuum states can evolve into particles. (The existence of stable bound states and physical scattering processes in such an environment is clearly far from trivial!). In our analysis spectral flow of this kind is directly introduced by the appearance of the triangle graph infra-red divergence in reggeized gluon interactions. It is interesting

---

<sup>§</sup>The conventional wisdom is probably that strong coupling confinement effects overwhelm such phenomena altogether. As we have emphasized elsewhere, we expect our discussion to apply to a weak coupling version of massless QCD in which there is, effectively at least, an infra-red fixed point.

that a related phenomenon has already been encountered in next-to-leading order calculations[14] of the high-energy scattering of massless gluons. A massless gluon triangle diagram occurs in the effective vertex for reggeized gluon exchange and produces a “particle/antiparticle transition” that for gluons is simply an unanticipated helicity transition.

A reggeon interaction vertex can be obtained by calculating the contribution of Feynman diagrams to the simplest multi-regge limit in which the vertex appears. In [10] we distinguished two methods for calculating multi-regge amplitudes - the direct calculation of diagrams in light-cone co-ordinates and the calculation of multiple asymptotic discontinuities with the subsequent use of an asymptotic dispersion relation. Although, the two methods should ultimately produce the same results, direct light-cone calculations are impractical for the problem we are discussing. This is because of the large number of diagrams that could contribute and because the complexity of the diagrams makes a full discussion of whether or not integration contours are truly trapped, in the asymptotic limits involved, very difficult. Consequently the asymptotic dispersion relation method has to be used. In this paper, therefore, we develop methods aimed at directly calculating multiple asymptotic discontinuities.

The form of the asymptotic dispersion relation for a given multi-regge process is determined by the possible asymptotic multiple discontinuities that satisfy the Steinmann relation property (that the discontinuities occur in non-overlapping invariant channels). Such discontinuities are explicitly reflected in the analytic structure of asymptotic amplitudes provided by multi-regge theory and, conversely, using the dispersion relation, multi-regge amplitudes can be calculated directly from the discontinuities. In [6] we described how the appearance of the anomaly pole in the elementary three current amplitude could be understood as due to an unphysical triangle landau singularity appearing (from an unphysical sheet) at the edge of the physical region. Correspondingly, the crucial feature of the high-order amplitudes that produce reggeon interactions containing the anomaly is the presence of unphysical multiple discontinuities that satisfy the Steinmann relation property and approach physical scattering regions only asymptotically. (This implies that they correspond to contour trappings that would be very difficult to demonstrate using direct light-cone calculations.) Discontinuities of this kind are present in complex (imaginary momentum) parts of the asymptotic region for sufficiently complicated many-particle multi-regge processes, the simplest of which is the full triple-regge region[8] that we study in this paper. Because they are in non-overlapping channels these discontinuities can (and must) consistently appear in the asymptotic amplitudes that describe also the real physical region behavior.

The familiar amplitudes that appear in multi-regge production processes (such as those that contribute to the BFKL equation[7]) do not contain unphysical multiple discontinuities. Rather they contain only multiple discontinuities that are naturally

interpreted as due to a succession of physical region on-shell scattering processes. (The necessity for a physical time-ordering of such processes then determines the absence of overlapping channel discontinuities.) Because physical region multiple discontinuities involve only physical amplitudes and physical intermediate states, when they are calculated using the perturbative amplitudes of the massless theory, they can not contain chirality transitions associated with particle/antiparticle ambiguities. Therefore, when only production processes are involved (i.e. at what we might call the BFKL level of multi-regge theory) there is no possibility for “chirality violation”.

A priori, there is no reason why unphysical multiple discontinuities should not contain potential chirality transitions when calculated perturbatively. Nevertheless, the occurrence of the infra-red anomaly within such discontinuities is very subtle. The divergence is produced by a quark loop that reduces to a triangle by the placing of many propagators on-shell. Of the three propagators associated with the triangle diagram, one must carry the zero momentum that allows a chirality transition while the other two carry the same light-like momentum. The additional on-shell propagators have to be associated with a triple discontinuity in such a way that (when all transverse momenta are zero) they also can all carry the same light-cone momentum (relative to the direction of the loop momentum). It is obvious that this requirement can not be satisfied by a physical triple discontinuity and, in fact, it is very difficult to satisfy. (As we briefly discuss towards the end of this paper, this difficulty is likely to be closely related to the complexity involved in having local interactions of the anomaly current appear in the ultraviolet region of reggeon interaction vertices.) Indeed, we will see that by itself this requirement is sufficient to ensure that (in the obtained reggeon interaction) at least three reggeons are present in each reggeon channel. Requiring that the spin structure that generates the anomaly also be present, then further restricts the contributing triple discontinuities to those originating from a small class of feynman diagrams. The discontinuities involved are truly unphysical in that they correspond to three “asymptotic pseudothresholds” (or, in more technical S-Matrix language, “mixed  $\alpha$  singularities”) each of which contains particles (effectively) going in opposite time directions. Not surprisingly, though, this provides just the right circumstances for the anomaly to appear.

As we noted above, the obtained reggeon interactions are of such high order that the minimum circumstances in which they can occur (between color zero reggeon states) is when each of the states involved carries the quantum numbers of the U(1) anomaly current. The lower-order diagrams considered in [10] remain valuable to discuss for illustrative processes but the analysis within this paper shows that they are essentially irrelevant. We do not give any detailed discussion of further cancelations amongst the diagrams we consider. We note, however, that the signature rule of [10] implies that the full vertex for three reggeon states, each of which carries the quantum numbers of the U(1) anomaly current, must vanish. In the pion/pomeron vertex

obtained in [6] there are, in addition to the three gluon reggeons, a quark/antiquark pair in the pion, and an additional reggeon in the pomeron. In the triple pomeron vertex, which we also briefly discuss, there is an additional reggeon in each channel. In following papers we hope to lay out the details of the construction of the full multi-regge S-Matrix alluded to above. For the moment we note only that triple-regge interactions of the kind we consider here will contribute generally to the vertices and interactions of the reggeon bound states that emerge and refer to the brief discussion in [10], and also to the outline in [12], for more details.

## 2. MULTIPLE DISCONTINUITIES AND THE STEINMANN RELATIONS.

### 2.1 Physical Region Discontinuities

The Steinmann relations originated in axiomatic field theory[15]. They (essentially) describe the restrictions that the time-ordering of interactions places on the combinations of intermediate states that can occur in a scattering process. For on-shell S-Matrix amplitudes their significance is most immediately appreciated in the approximation that we ignore higher-order Landau singularities and consider only the normal threshold branch points (and stable particle poles) that occur in individual channel invariants. The Steinmann relations then say that simultaneous thresholds (and/or poles) can not occur in overlapping channels. (Channels overlap if they contain a common subset of external particles.) As a result an  $N$ -point amplitude has at most  $N - 3$  simultaneous cuts (or poles) in distinct invariants. The possible combinations of cuts can be described by tree diagrams with three-point vertices in which each internal line corresponds to a channel invariant in which there is a cut due to intermediate state thresholds - as illustrated in Fig. 2.1 for the 7-point amplitude.

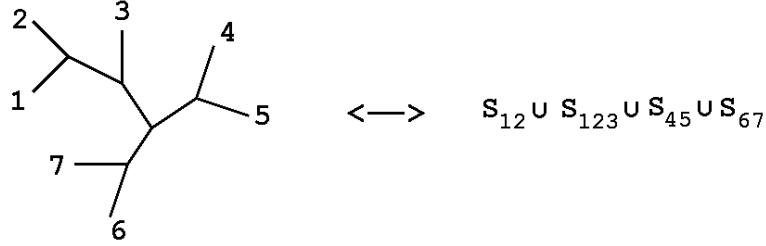


Fig. 2.1 A Tree Diagram Representing Simultaneous Invariant Cuts.

(As usual,  $s_{12} = (P_1 + P_2)^2$ ,  $s_{123} = (P_1 + P_2 + P_3)^2$ , etc.) The set of all combinations of thresholds (and poles) allowed by the Steinmann relations is the basic singularity structure of all scattering amplitudes. The higher-order Landau singularities are believed[16] to emerge from the normal thresholds in a manner that, for most purposes, makes them a secondary effect.

Conversely, the combination of cuts represented by a particular tree diagram can be directly associated with a set of physical scattering processes. As illustrated in Fig. 2.2, this is the set of all processes (involving all the external particles of the diagram as either ingoing or outgoing particles) in which it is kinematically possible for all of the internal lines to be replaced by physical multiparticle states<sup>¶</sup>.

<sup>¶</sup>We do not distinguish processes in which ingoing and outgoing particles are interchanged via



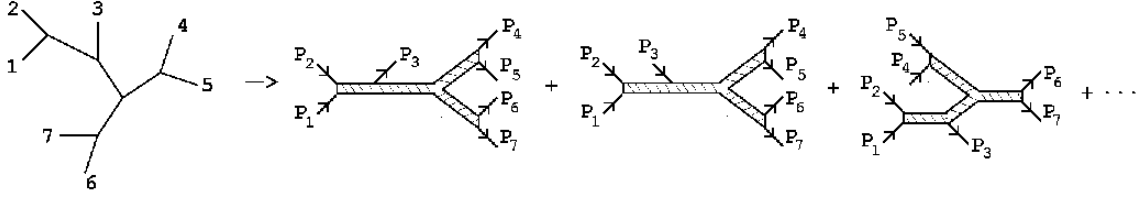


Fig. 2.2 Physical Scattering Processes Corresponding to Fig. 2.1.

The hatched segments represent physical intermediate states that, if they are all placed on shell, give (essentially) the associated multiple discontinuity.

The Steinmann relations play a fundamental role in multi-regge theory. It is possible to show[16] that in a physical multi-regge asymptotic region the analytic structure of scattering amplitudes can be treated as if only normal thresholds satisfying the Steinmann relations were present. In effect, higher-order Landau singularities are suppressed. This has the very important consequence that only the normal threshold cuts in individual channel invariants need be represented by multi-regge asymptotic formulae. Furthermore, if we consider only the multi-regge limits accessible in  $2 \rightarrow M$  production processes, it can be shown that the maximal number  $(M-1)$  of simultaneous thresholds is encountered asymptotically only in physical regions. This is a generalization of the cut-plane analyticity property familiar from elastic scattering.

## 2.2 Unphysical Multiple Discontinuities

If we consider the multi-regge regions of  $M \rightarrow M'$  scattering amplitudes ( $M, M' \geq 3$ ) there is a significant change. To understand the point involved consider the simplest case of the tree diagram of Fig. 2.3. At first sight this diagram corresponds only to the  $2 \rightarrow 4$  production processes shown.

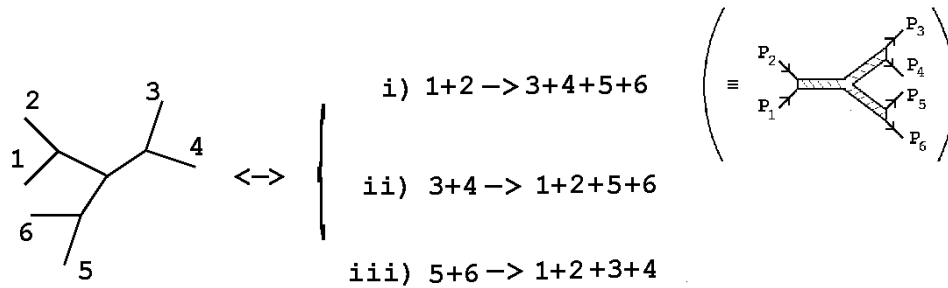


Fig. 2.3 A Tree Diagram and Corresponding Physical Scattering Processes.

The three distinct scattering processes are distinguished by different constraints on  


---

CPT conjugation

the invariants, i.e.

$$\begin{aligned}
\text{i)} \quad & \sqrt{s_{12}} > \sqrt{s_{34}} + \sqrt{s_{56}} , \\
\text{ii)} \quad & \sqrt{s_{34}} > \sqrt{s_{12}} + \sqrt{s_{56}} , \\
\text{iii)} \quad & \sqrt{s_{56}} > \sqrt{s_{12}} + \sqrt{s_{34}}
\end{aligned} \tag{2.1}$$

We can also regard the three processes involved as distinguished by the selection of one pair of particles as incoming, which then must have energy larger than the sum of the subenergies of the other two pairs, which are necessarily in the outgoing state.

We may wonder about the symmetric asymptotic region in which

$$\sqrt{s_{12}} \sim \sqrt{s_{34}} \sim \sqrt{s_{56}} \rightarrow \infty \tag{2.2}$$

There are no physical scattering processes in this region. However, the three processes of (2.1) are described by the same (analytically continued) amplitude and so analytic continuation from each of the physical regions implies that such cuts must be present. It is, perhaps, natural that a triple discontinuity should exist that is symmetric with respect to the three processes of Fig. 2.3. Apparently, though, the symmetry requirement could only be satisfied if all the external particles are in the final, or initial, state. In fact, as we discuss further in the next Sections, if we allow particles to carry complex momenta, a positive value for a two-particle energy invariant can be achieved by a combination of an “incoming” and an “outgoing” particle in that they carry opposite sign, but imaginary, energies. Therefore, in the symmetric region it is possible for the three cuts of Fig. 2.3 to be present if each is associated with such a combination. We will show in the following that there are unphysical processes (with imaginary momenta) in this region that do produce a triple discontinuity of this kind and we will refer to it as an “unphysical triple discontinuity”.

Since the external particles for each cut are both ingoing and outgoing it is, perhaps, not surprising that intermediate states appear that also involve such combinations. Indeed, we will see that this is how a triple discontinuity can contain the “particle - antiparticle” transitions that ultimately provide the massless chirality transitions that we are looking for. Since the complex momentum part of (2.2) is contained in the triple-regge asymptotic region, a triple discontinuity of this kind is just what we are looking for. The importance of the triple-regge region is that it is the simplest multi-regge limit in which the vertices appear that provide the couplings of bound-state regge poles such as the pomeron or the pion. For higher-point  $M \rightarrow M'$  amplitudes there is a wide range of unphysical multiple discontinuities satisfying the Steinmann relations. Bound-state scattering amplitudes can thus appear in which the anomaly is a crucial element.

### 3. THE PHYSICAL REGION ANOMALY AND THE TRIPLE-REGGE DISPERSION RELATION

#### 3.1 The Triple Regge Limit and Maximally Non-Planar Diagrams

In our previous paper[10] we studied the full triple-regge limit[8] of three-to-three quark scattering. If we denote the initial momenta as  $P_i$ ,  $i = 1, 2, 3$ , and the final momenta as  $-P_{i'} = P_i + Q_i$ ,  $i = 1, 2, 3$ , the triple-regge limit can be realized, within the physical region, by taking each of  $P_1$ ,  $P_2$  and  $P_3$  large along distinct light-cones, with the momentum transfers  $Q_1, Q_2$  and  $Q_3$  kept finite, i.e.

$$\begin{aligned} P_1 \rightarrow P_{1+} &= (p_1, p_1, 0, 0), \quad p_1 \rightarrow \infty & q_1 = Q_1/2 &\rightarrow (\hat{q}_1, \hat{q}_1, q_{12}, q_{13}) \\ P_2 \rightarrow P_2^+ &= (p_2, 0, p_2, 0), \quad p_2 \rightarrow \infty & q_2 = Q_2/2 &\rightarrow (\hat{q}_2, q_{21}, \hat{q}_2, q_{23}) \\ P_3 \rightarrow P_3^+ &= (p_3, 0, 0, p_3), \quad p_3 \rightarrow \infty & q_3 = Q_3/2 &\rightarrow (\hat{q}_3, q_{31}, q_{32}, \hat{q}_3) \end{aligned} \quad (3.1)$$

Momentum conservation gives a total of five independent  $q$  variables which, along with  $p_1, p_2$  and  $p_3$ , give the necessary eight variables. The definition of the triple-regge limit in terms of angular variables is given in [10]. For our present purposes the above definition in terms of momenta will be sufficient. This will allow us to avoid the extra complication of defining helicity angles, helicity-pole limits etc. The asymptotic behavior involved must hold for all complex values of the large momenta, including the additional physical regions reached by reversing the signs of the  $p_i$ .

In [10] we also studied feynman diagrams that contain a closed quark loop and generate triple-regge reggeized gluon interactions containing the loop. To set the context for the present paper we briefly review the results. We considered the lowest-order amplitudes in which the anomaly could potentially appear and, in particular, studied “maximally non-planar” diagrams of the kind shown in Fig. 3.1(a).

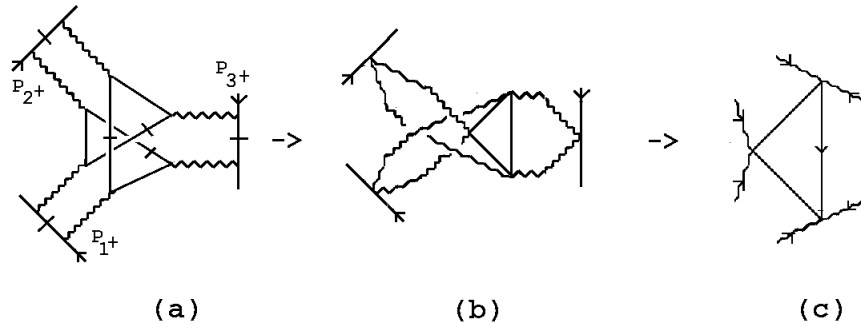


Fig. 3.1 A maximally non-planar diagram and the triangle diagram reggeon interaction produced.

(Throughout this paper we adopt the usual convention that solid and wavy lines respectively represent a quark and a gluon. We have reversed the direction of  $P_3$  relative to the notation of [10] in order to have a completely symmetric notation.) The leading asymptotic contributions come from regions of gluon loop integrations where some of the propagators in the quark loop and the scattering quark systems are on-shell. We discuss the determination of which propagators can be on-shell below. For the moment we consider the possibility, discussed at length in [10], that the on-shell lines are those that are hatched in Fig. 3.1(a). We will eventually conclude that this combination of on-shell propagators can not produce a reggeon interaction with a physical region anomaly divergence, even though it does produce a triangle diagram interaction. As we will see, the crucial issue is not just which propagators are placed on-shell but also which pole (“particle” or “antiparticle”) is involved. (As the discussion in the previous Section suggested, for the unphysical discontinuities, with which we will ultimately be concerned, the answer to this question is not unambiguous.) In the following we initially ignore this subtlety. As it emerges in our discussion it will become clear that it is a vital part of the search for further diagrams which do produce an interaction containing the anomaly.

If the hatched on-shell propagators are used to carry out light-like longitudinal momentum integrations the integrals over gluon loop momenta reduce to two-dimensional “transverse” integrals over spacelike momenta, as illustrated by Fig. 3.1(b). The transverse plane (and orthogonal light-like momenta) can, in general, be chosen differently in each  $t$ -channel. If  $Q_{i\perp}$  is the projection of  $Q_i$  on the corresponding transverse plane, the leading asymptotic contribution then has the form

$$P_{1+} P_{2+} P_{3+} \prod_{i=1}^3 \int \frac{d^2 k_{i1} d^2 k_{i2}}{k_{i1}^2 k_{i2}^2} \delta^2(Q_{i\perp} - k_{i1} - k_{i2}) G_i^2(k_{i1}, k_{i2}, \dots) \times R^6(Q_1, Q_2, Q_3, k_{11}, k_{12}, \dots) \quad (3.2)$$

where  $R^6(Q_1, Q_2, Q_3, k_{11}, k_{12}, \dots)$  can be identified with the “reduced”, or “contracted”, feynman diagram of Fig. 3.1(c). If we write

$$k_{i1} = q_i + k_i, \quad k_{i2} = q_i - k_i, \quad (3.3)$$

then we showed in [10] that (with a particular choice of transverse planes)

$$R^6(q_1, q_2, q_3, k_1, k_2, k_3) = \int d^4 k \frac{\text{Tr}\{\gamma_5 \gamma^{-, -, +} (\not{k} + \not{k}_1 + \not{q}_2 + \not{k}_3) \gamma_5 \gamma^{-, -, -} \not{k} \gamma_5 \gamma^{-, -, -} (\not{k} - \not{k}_2 + \not{q}_1 + \not{k}_3)\}}{(k + k_1 + q_2 + k_3)^2 k^2 (k - k_2 + q_1 + k_3)^2} + \dots \quad (3.4)$$

where

$$\gamma^{\pm, \pm, \pm} = \gamma^\mu \cdot n_\mu^{\pm, \pm, \pm}, \quad n_\mu^{\pm, \pm, \pm} = (1, \pm 1, \pm 1, \pm 1) \quad (3.5)$$

The contributions to  $R^6$  not shown explicitly in (3.4) do not have a  $\gamma_5$  at all three vertices of the triangle diagram. As we will discuss again in Section 5, the particular  $\gamma$ -matrix projections appearing depend on the choice of transverse co-ordinates. If the anomaly is present in  $R^6$ , however, we expect it to be independent of this choice. We should emphasize that while we have written (3.4) as a function of four-dimensional momenta, the  $k_i$  are restricted to be two-dimensional spacelike momenta (plus longitudinal components determined by the mass-shell conditions for the on-shell quarks) and the  $q_i$  have the restricted form given by (3.1). These restrictions play a crucial role in determining whether the anomaly can occur in a physical region reggeon interaction.

### 3.2 A Reggeon Diagram Amplitude

For completeness, we give a brief description (full details can be found in [10]) of how a reggeon vertex is extracted from (3.2). A reggeon diagram amplitude that represents right-hand cuts in the unphysical triplet  $\{s_{13'}, s_{32'}, s_{21'}\}$  and has two reggeons in each  $t$ -channel, each with trajectory  $\alpha(t) = 1 + O(g^2)$ , has the form[10]

$$\prod_i \int \frac{d^2 k_i}{\sin \pi \alpha(k_i^2) \sin \pi \alpha((Q_i - k_i)^2)} \beta(k_1, k_2, k_3, Q_1, Q_2, Q_3) \left[ \begin{aligned} & (s_{13'})^{[\alpha(k_1^2) + \alpha((Q_1 - k_1)^2) + \alpha(k_3^2) + \alpha((Q_3 - k_3)^2) - \alpha(k_2^2) - \alpha((Q_2 - k_2)^2) - 1]/2} \\ & (s_{32'})^{[\alpha(k_3^2) + \alpha((Q_3 - k_3)^2) + \alpha(k_2^2) + \alpha((Q_2 - k_2)^2) - \alpha(k_1^2) - \alpha((Q_1 - k_1)^2) - 1]/2} \\ & (s_{21'})^{[\alpha(k_1^2) + \alpha((Q_1 - k_1)^2) + \alpha(k_2^2) + \alpha((Q_2 - k_2)^2) - \alpha(k_3^2) - \alpha((Q_3 - k_3)^2) - 1]/2} \end{aligned} \right] \quad (3.6)$$

$$\left[ \begin{aligned} & \left[ \sin \frac{\pi}{2} [\alpha(k_1^2) + \alpha((Q_1 - k_1)^2) + \alpha(k_3^2) + \alpha((Q_3 - k_3)^2) - \alpha(k_2^2) - \alpha((Q_2 - k_2)^2)] \right. \\ & \sin \frac{\pi}{2} [\alpha(k_3^2) + \alpha((Q_3 - k_3)^2) + \alpha(k_2^2) + \alpha((Q_2 - k_2)^2) - \alpha(k_1^2) - \alpha((Q_1 - k_1)^2)] \\ & \left. \sin \frac{\pi}{2} [\alpha(k_1^2) + \alpha((Q_1 - k_1)^2) + \alpha(k_2^2) + \alpha((Q_2 - k_2)^2) - \alpha(k_3^2) - \alpha((Q_3 - k_3)^2)] \right]^{-1} \\ & \sim (s_{13'})^{1/2} (s_{32'})^{1/2} (s_{21'})^{1/2} \prod_i \int \frac{d^2 k_i}{k_i^2 (Q_i - k_i)^2} \beta(k_1, k_2, k_3, Q_1, Q_2, Q_3) \end{aligned} \right] \quad (3.7)$$

$g^2 \rightarrow 0$

(The generalization of this formula to include more reggeons in any of the channels should be obvious.) Taking the triple discontinuity in  $s_{13'}$ ,  $s_{32'}$  and  $s_{21'}$  of (3.6) removes the poles due to the sine factors in the second square bracket, but leaves the  $g^2 \rightarrow 0$  limit unchanged. Since the triple discontinuity is unphysical and of the kind discussed in the previous Section, according to the discussion in [10], the “six-reggeon interaction vertex”  $\beta(k_1, k_2, k_3, Q_1, Q_2, Q_3)$  could contain the anomaly.

Writing

$$P_{1+}P_{2+}P_{3+} \equiv (s_{13'})^{1/2}(s_{32'})^{1/2}(s_{21'})^{1/2} \quad (3.8)$$

and comparing with (3.7) we see that it would be straightforward to identify (3.2) as a lowest-order contribution to such a reggeon diagram amplitude if the reduced feynman diagram amplitude of Fig. 3.1(c) is identified as a reggeon vertex, i.e.

$$R^6(Q_1, Q_2, Q_3, k_1, Q_1 - k_1, \dots) \equiv \beta(k_1, k_2, k_3, Q_1, Q_2, Q_3) \quad (3.9)$$

Note, however, that while the right-side of (3.8) clearly has a triple discontinuity in  $\{s_{13'}, s_{32'}, s_{21'}\}$ , the left-side does not. The equivalence of the two sides is only determined if higher-order terms in (3.6) appear and add to (3.2) in the appropriate manner. Such terms are contributed by what we refer to in the following as reggeization diagrams. Note, also, that for parts of  $R^6$  (not including  $\gamma_5$  couplings) higher-order terms would be expected to appear implying that, one or more of, the transverse integrals in (3.2) should be interpreted as arising from the trajectory function terms in (3.6). Such parts of  $R^6$  would then be interpreted as providing interaction vertices for fewer reggeons.

The amplitude (3.4) representing Fig. 3.1(c) is the full four-dimensional triangle diagram amplitude except that special  $\gamma$ -matrices appear at the vertices and only combinations of (essentially) two-dimensional transverse momenta flow through the diagram. It is shown in [10] that the  $\gamma$ -matrix couplings are appropriate to produce the anomaly but, as we discuss next, whether the necessary momentum configuration can occur within a physical region and provide a physical region infra-red divergence is a non-trivial and subtle question that depends crucially on the choice of propagator poles used to put lines on-shell.

### 3.3 The Basic Anomaly Process

As we discuss further in Section 5, the divergence of the (massless) triangle diagram occurs[6] when a single light-like momentum flows through the diagram and all other momenta are spacelike and scaled to zero. Such a momentum configuration for the reggeon interaction  $R$  is realized by that of the full feynman diagram shown in Fig. 3.2(a). If we label the momenta entering the reggeon interaction as in Fig. 3.2(b) an explicit configuration for Fig. 3.2(a), discussed in [10], is

$$q_1 - k_1 = (2l, 2l, 0, 0), \quad q_2 - k_2 = (-2l, 0, -2l, 0) \quad (3.10)$$

together with

$$\hat{q}_1 = -\hat{q}_2 = l \quad q_{13} = -q_{23} \quad q_{12} = q_{21} = 0 \quad (3.11)$$

This determines  $k_1$  and  $k_2$  and also gives

$$q_3 = -(q_1 + q_2) = (0, -l, l, 0) \quad (3.12)$$

If we then take

$$k_3 = l(0, 1 - 2 \cos \theta, 1 - 2 \sin \theta, 0) \quad (3.13)$$

the light-cone momentum

$$- 2l(1, \cos \theta, \sin \theta, 0) \quad (3.14)$$

flows along the two vertical non-hatched lines in Fig. 3.2(b). It is straightforward to check that all three of the hatched lines are on mass-shell.

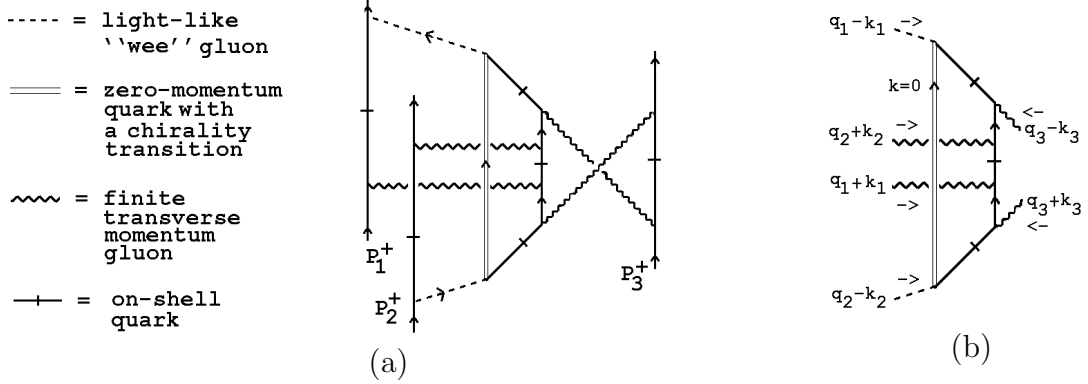


Fig. 3.2 The basic anomaly process.

If spacelike momenta of  $O(q)$  are added to the momentum configuration (3.10)-(3.14) and the limit  $q \rightarrow 0$  is taken, the anomaly divergence occurs. (We will discuss this in more detail in Section 5.)

Apart from the reversal of direction for  $P_3$ , the process represented by Fig. 3.2(a) is what we called “the basic anomaly process” in [10]. The zero momentum quark is produced by one “wee gluon” and absorbed by the other, allowing the chirality transition produced by the anomaly to compensate for a spin flip of the antiquark. Note, however, that when the wee gluons are massless, the scattering process represented by Fig. 3.2 is physical only when the quark and antiquark involved are also massless. In addition, as we noted in the Introduction (and discussed in more detail in [6], the anomaly infra-red divergence involves both poles of the zero momentum quark propagator. Moreover, the vertices coupling to the propagator should, a priori, be symmetrically interpreted as describing either the simultaneous production of the two states in the propagator or their simultaneous absorption. When, as is the case in [6], the infra-red divergence analysis used to define physical states and amplitudes requires that the massless scattering enter the physical region with the time ordering implied by Fig. 3.2, the presence of a non-perturbative background gauge field is effectively implied. The background field would be needed to produce the necessary spectral flow at one vertex that is required to interpret the process as a chirality transition.

While the required mass-shell conditions are indeed satisfied by (3.10)-(3.14), there is a problem. With the momenta given by (3.10)-(3.14), the energy component of each of the three hatched lines in Fig. 3.2(b) has the same sign. Since the exchanged gluons carry only spacelike momenta, it is clear that this must be the case. We will see that this is a very difficult configuration to obtain within a reggeon interaction. We can emphasize the problem by letting  $l \rightarrow 0$  while simultaneously making a boost  $a_z(\zeta)$  such that  $l \cosh \zeta = n$  is kept finite. (This is what is done in [6].) If we then take all transverse momenta to zero, we obtain

$$q_1 - k_1 \rightarrow (2n, 0, 0, 2n), \quad q_2 - k_2 \rightarrow (-2n, 0, 0, -2n) \quad (3.15)$$

and all the on-shell propagators carry the same light-like momentum (with respect to the direction of the loop momentum). Effectively, then, the on-shell states in the loop must be in a symmetric light-like situation. (This implies that if the zero momentum state is an antiquark (quark), all hatched lines must be quarks (antiquarks).)

As we already remarked on in the Introduction, and as is discussed at length in [10], the only practicable calculational method to determine whether a given combination of on-shell lines contributes to the triple-regge behavior (after all diagrams are added) is the dispersion relation method that we outline very briefly below. In this approach all on-shell lines in a reggeon interaction result directly from the taking of a triple asymptotic discontinuity. “Real part” interactions with the same on-shell lines may be generated when the full dispersion relation is written or, equivalently, multi-regge theory is used[10] to convert the triple discontinuity to a full amplitude.

To have all on-shell lines carry the same light-like momentum (around a loop) in a multiple discontinuity is a very restrictive requirement. The essential point becomes clear if we consider a physical region double discontinuity which gives the cut lines of Fig. 3.1(a), as in Fig. 3.3(a).

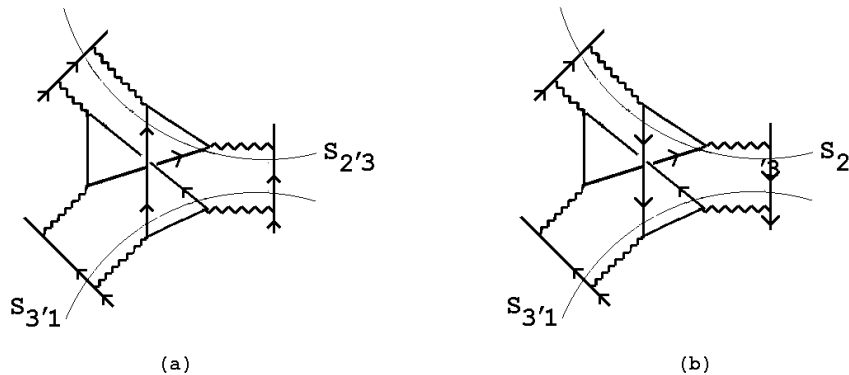


Fig. 3.3 (a) A physical threshold double discontinuity (b) A pseudothreshold double discontinuity.



If all cut lines carry light-like momenta, the positive direction for the energy component must be as indicated by the arrows in Fig. 3.3(a). Obviously the direction can not be the same, relative to the internal loop momentum, for all cut lines. Nevertheless, this is an essential requirement if a reggeon interaction is to contain a physical region divergence produced by the anomaly (i.e. some variant of the “basic anomaly process” must be involved). We obtain what we require if we reverse one internal line and one external line (to make the cutting completely symmetric) as in Fig. 3.3(b). Since both cuts now involve both forward and backward going (in time) particles it is clear that we must have a combination of pseudothresholds, just as suggested in the previous Section, that can occur only in an unphysical region of momentum space.

We already recognized in [10] that the necessary triple discontinuity is not present in the diagram of Fig. 3.1 but we suggested that nevertheless it may be present in related higher-order reggeization diagrams that produce the reggeization of the gluons. In which case, the basic anomaly process of Fig. 3.2 would be required as a real part interaction. In fact, we will show in the remaining part of this paper that this is not the case. Instead, the requirement that all cut lines are treated symmetrically will require more wee gluons and ultimately will require that reggeon interactions with the quantum numbers of the winding number current must be involved. Also, as we already anticipated in the previous Section the discontinuities involved must be unphysical.

As we discussed in [10], we do not expect the anomaly divergence to be present in the scattering of elementary quarks and/or gluons after all diagrams are summed. Rather, we expect it to be present when the basic process is generalized to describe the scattering of the particular multi-regge states that ultimately form bound states, and then only in color superconducting QCD. In [6] it is clear that the relevant bound-states are just the Goldstone bosons produced by chiral symmetry breaking. The corresponding  $G_i$  will then appear in a generalization of (3.2) and the wee gluons involved will be a crucial characteristic of scattering states. Also the chirality transitions produced (and the implicit spectral flow) will be an essential part of scattering processes.

### 3.4 The Triple-Regge Dispersion Relation

In general, an asymptotic dispersion relation[16] gives the leading multi-regge behavior of an amplitude as a sum over multiple discontinuity contributions allowed by the Steinmann relations. For the particular case (described in detail in [10]) of the triple-regge behavior of a six-point amplitude we can write

$$M_6(P_1, P_2, P_3, Q_1, Q_2, Q_3) = \sum_c M_6^c(P_1, P_2, P_3, Q_1, Q_2, Q_3) + M_6^0, \quad (3.16)$$

where  $M_6^0$  contains all non-leading triple-regge behavior, double-regge behavior, etc.

and the sum is over all triplets  $\mathcal{C}$  of asymptotic cuts in non-overlapping (large) invariants. For each triplet  $\mathcal{C}$ , say  $\mathcal{C} = (s_1, s_2, s_3)$ , we can write

$$M_6^{\mathcal{C}}(P_1, P_2, P_3, Q_1, Q_2, Q_3) = \frac{1}{(2\pi i)^3} \int ds'_1 ds'_2 ds'_3 \frac{\Delta^{\mathcal{C}}}{(s'_1 - s_1)(s'_2 - s_2)(s'_3 - s_3)} \quad (3.17)$$

where  $\Delta^{\mathcal{C}}$  is the triple discontinuity.

The triple discontinuities are of three kinds, described by the tree diagrams of Fig. 3.4. There are 24 corresponding to Fig. 3.4(a), 12 to Fig. 3.4(b), and 12 of the Fig. 3.4(c) kind - including those described by Fig. 2.3. Those of Fig. 3.4(a) and (b), occur in the physical regions, while those corresponding to Fig. 3.4(c) are all unphysical triple discontinuities of the kind discussed in the last Section.

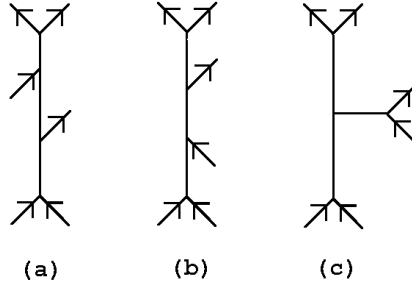


Fig. 3.4 Tree Diagrams for triple discontinuities.

### 3.5 Unphysical Triple Discontinuities and Reggeization

As we discussed in [10], the diagram of Fig. 3.1(a) has physical region triple discontinuities of both the Fig. 3.4(a) and (b) kinds, although neither gives leading triple-regge behavior. Unphysical discontinuities are more complicated to discuss. If the usual cutting rules hold, the diagram of Fig. 3.1(a) has no asymptotic triple discontinuities corresponding to Fig. 3.4(c), but rather has only double discontinuities. To see this, consider cutting the diagram as in Fig. 3.5, superficially giving an  $\{s_{13'}, s_{32'}, s_{21'}\}$  triple discontinuity.

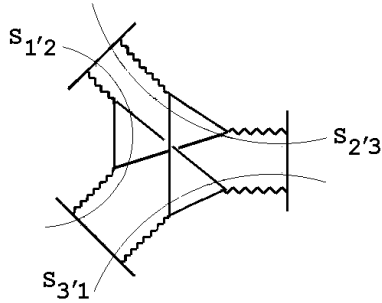


Fig. 3.5 An unphysical triple discontinuity?

In fact, just taking a double discontinuity, as in Fig. 3.3, cuts all the available lines, implying that there is no independent third discontinuity that can be taken.

It is not clear, a-priori, that the cutting rules do apply to unphysical discontinuities. However, we will show directly in the next Section that, indeed, there is no symmetric triple discontinuity present giving the desired common energy component sign in the diagram of Fig. 3.1. Therefore, as we described above, whether there is an anomaly contribution from diagrams of this kind depends on whether the necessary triple discontinuities are present when reggeization effects appear. In [10] we noted only that such discontinuities appeared to be present in reggeization diagrams but did not discuss the structure of such diagrams in any detail.

As an example of a diagram that should produce reggeization, consider that shown in Fig. 3.6

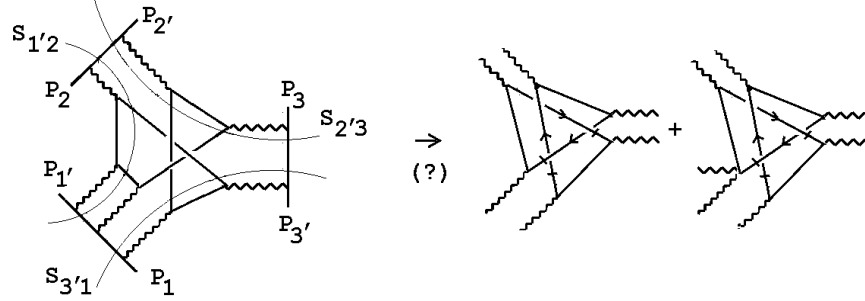


Fig. 3.6 A diagram with an unphysical triple discontinuity.

in which one of the gluons in the diagram of Fig. 3.5 is replaced by two-gluon exchange - potentially giving the one-loop contribution to the trajectory function of the original gluon. The thin lines again indicate how an unphysical  $\{s_{13'}, s_{32'}, s_{21'}\}$  discontinuity would be taken. The corresponding six reggeon interaction, together with a remnant seven reggeon interaction, would be generated by putting the cut lines on-shell. The discontinuity is clearly not symmetric and in the next Section we will confirm by direct calculation that there is no triple discontinuity giving the anomaly. This will be sufficient to determine that the anomaly process of Fig. 3.2 is not generated as a “real part interaction” when higher-order reggeization effects are included.

### 3.6 A Symmetric Triple Discontinuity

To obtain a symmetric triple discontinuity in which the normal cutting rules could potentially give the anomaly amplitude associated with Fig. 3.2, we consider the high-order diagram shown in Fig. 3.7(a) in which there are three gluons in each  $t$ -channel. A triple discontinuity in  $\{s_{1'2}, s_{2'3}, s_{3'1}\}$  is obtained by cutting the diagram

as indicated in Fig. 3.7(b). The closed loops involving two-gluon exchange could give both one loop contributions to the one reggeon trajectory function and the leading contribution of a two reggeon state. A-priori, therefore, we expect the diagram to contribute to the six-, seven-, eight- and nine-reggeon interaction as illustrated.

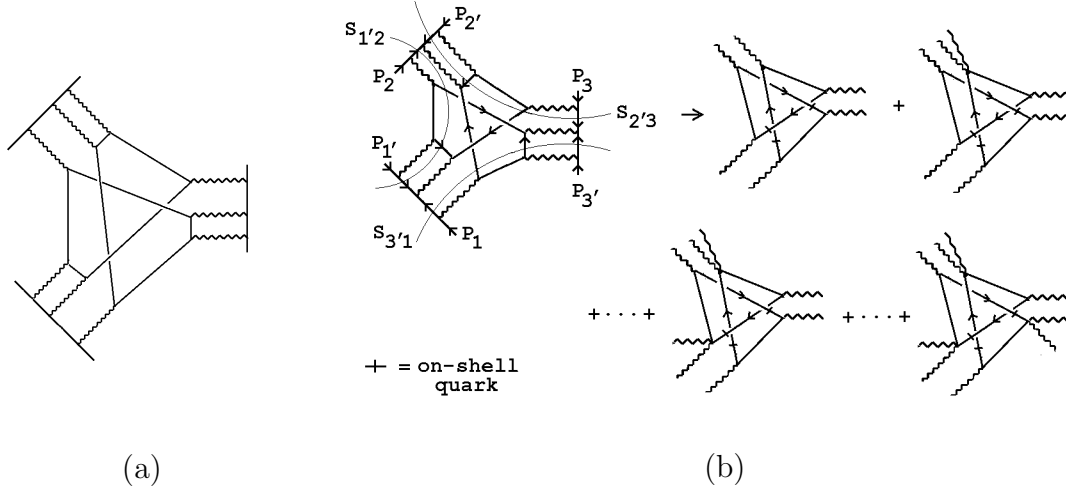


Fig. 3.7 (a) A diagram with a symmetric unphysical triple discontinuity  
(b) expected reggeon interactions.

Since the triple discontinuity of Fig. 3.7(b) is manifestly symmetric we again might expect the symmetric configuration giving the anomaly to appear in the six-reggeon interaction. However, for consistency with our previous discussion, the anomaly should not (and does not) appear quite so simply. After we carry out the explicit evaluation of asymptotic discontinuities in the next Section, it will be clear that the triple discontinuity of Fig. 3.7(b) does not contain the required symmetric momentum configuration. In fact, the anomaly does occur within a reggeon interaction generated by the diagram of Fig. 3.7(a), but only when the unphysical discontinuities are actually taken as shown in Fig. 3.8.

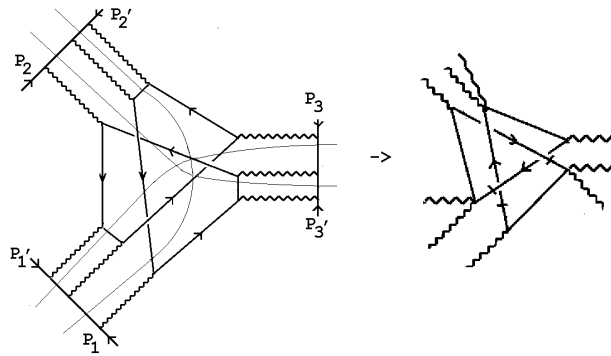


Fig. 3.8 Another cutting of Fig. 3.7(a).

However, we will postpone until Section 5 a discussion of which reggeon interaction is involved. Note that the discontinuity lines in Fig. 3.8 cross each other. We will see that this is possible because, as anticipated in the previous Section, the particles contributing to each discontinuity will not all have the same time direction. To evaluate a multiple discontinuity of this kind we must develop direct methods to compute asymptotic discontinuities.

## 4. UNPHYSICAL TRIPLE DISCONTINUITIES AND HIGHER-ORDER GRAPHS

In this Section we generalize the single asymptotic discontinuity analysis described in the Appendix to asymptotic triple discontinuities. The essential idea is that there is a well-defined leading-log result for each triple discontinuity (just as there is for the single discontinuity calculated in the Appendix) that can be found from the leading-log calculation of amplitudes by keeping the  $i\epsilon$  dependence of all logarithms.

### 4.1 A Physical Region Discontinuity

We begin by considering again the maximally non-planar graph shown in Fig. 3.1. To understand how asymptotic discontinuities arise, we first consider a physical region discontinuity. For this we interchange  $P_1$  and  $P_{1'}$  in (3.1) so that  $P_{1'}$  and  $P_2$  are the momenta of incoming particles. For simplicity, we also set  $Q_i = 0$ ,  $i = 1, 2, 3$ . This could cause confusion as to which invariants discontinuities actually occur in. However, for the discontinuities that interest us, we will be able to avoid this issue. (As is the case for our discussion in the Appendix, adding both transverse momenta and masses to our discussion would not change the essential features of the analysis, but would eliminate gluon infra-red divergences. We will discuss, at some points, the general effect of adding transverse momenta.) Therefore we write, asymptotically,

$$\begin{aligned} P_{1'} &\rightarrow -P_1 = (p_{1'}, p_{1'}, 0, 0) , & p_{1'} &\rightarrow \infty \\ P_2 &\rightarrow -P_{2'} = (p_2, 0, p_2, 0) , & p_2 &\rightarrow \infty \\ P_3 &\rightarrow -P_{3'} = (p_3, 0, 0, p_3) , & p_3 &\rightarrow \infty \end{aligned} \tag{4.1}$$

For the reasons given in the last Section, we will ultimately be looking for a symmetric triple discontinuity. Therefore, we consider only routes for the internal loop momenta of Fig. 3.1 that are completely symmetric with respect to the three external loops. There is essentially only one possibility. The two apparently distinct possibilities illustrated in Fig. 4.1 are related by interchanging the primed and unprimed external momenta. We will also want to make a symmetric choice for the quark lines we place on shell. Although we will not discuss the anomaly in detail until the next Section, in anticipation of this we will demand that a product of three orthogonal  $\gamma$ -matrices be associated with the process of putting on-shell each internal quark line. To achieve this it is necessary to put on-shell, symmetrically, the internal lines in Fig. 4.1(a) along which a single loop momentum flows. Therefore, we consider only such lines in the following.

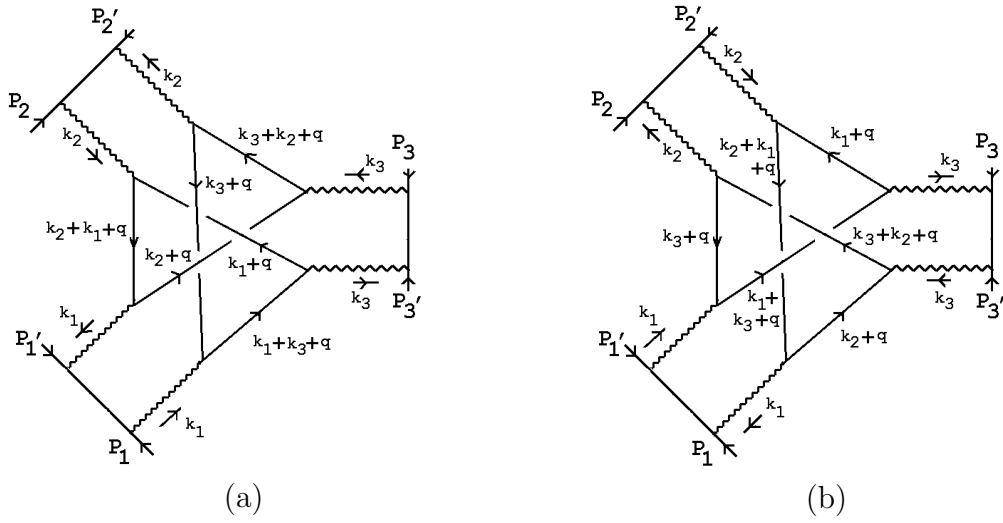


Fig. 4.1 Routing Loop Momenta for Fig. 3.2.

Using the momentum routing of Fig. 4.1(a) and the analysis of the Appendix we consider logarithms generated by the  $k_1$  and  $k_2$  integrations. The  $k_1$  and  $k_2$  loops are shown in Fig. 4.2.

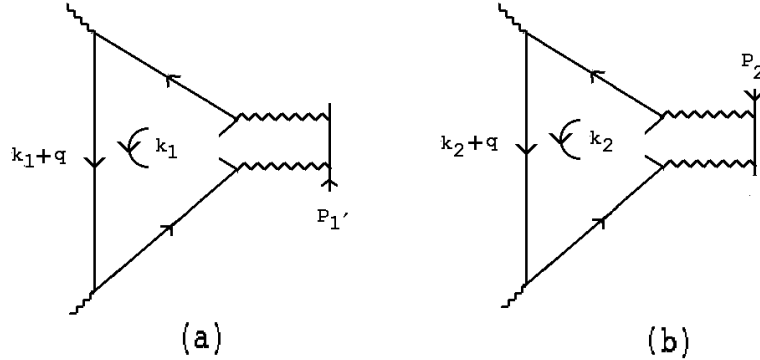


Fig. 4.2 (a) The  $k_1$  Loop (b) The  $k_2$  Loop.

For the moment, we omit the propagators in the sloping lines and all propagator numerators. (The omitted propagators will, nevertheless, play an important role below. They are also relevant if we wish to consider the other kinds of discontinuities that appear in Fig. 3.4.) In this case, the two loops differ only in the light-cone direction of  $P_1'$  and  $P_2$ .

We consider Fig. 4.2(a) first. We can directly apply the discussion following (A.4) if we identify  $P_1'$  with  $p$ ,  $q$  with  $p'$ ,  $k_1$  with  $k$ , and consider the propagator pole

at  $(k_1 + q)^2 = 0$ . We then obtain

$$\begin{aligned} I(p_1' q_{1-}) &\sim i \int d^2 \underline{k}_{1\perp} \left[ -k_{1\perp}^2 + i\epsilon \right]^{-2} \int_0^{\lambda q_{1-}} dk_{1-} [k_{1-} - q_{1-}]^{-1} \left[ p_1' k_{1-} - \underline{k}_{1\perp}^2 + i\epsilon \right]^{-1} \\ &\sim \frac{1}{p_1' q_{1-}} \log [p_1' \lambda q_{1-} + i\epsilon] \end{aligned} \quad (4.2)$$

We have used the notation (used extensively in the following) that for any four-momentum  $k$

$$k_{i\pm} = k_0 \pm k_i \quad \underline{k}_{i\perp} = (k_j, k_k) \quad j \neq k \neq i \quad i, j, k = 1, 2, 3 \quad (4.3)$$

The  $q_{1-}$  dependence indicates that the logarithm is a reflection of a threshold in the invariant  $P_1' \cdot q$ . This dependence plays an important role in the following discussion. We also retain the  $\lambda$ -dependence, for technical reasons that will become apparent later. The final result will be independent of  $\lambda$ , as it must be. From Fig. 4.2(b) we analogously obtain

$$I(p_2 q_{2-}) \sim \frac{1}{p_2 q_{2-}} \log [-p_2 \lambda q_{2-} + i\epsilon] \quad (4.4)$$

The minus sign (which is very important in the following) appears relative to (4.2) because of the opposite direction of  $P_2$ .

Next we consider how the logarithmic branch cuts generated by the  $k_1$  and  $k_2$  integrations can trap the internal loop integration over  $q$  to produce an overall discontinuity in  $s_{1'2} \sim p_1' p_2$ . For simplicity, we consider the region where

$$\underline{k}_{i\perp}^2 \sim q^2 \sim 0 \quad i = 1, 2, 3 \quad (4.5)$$

Appealing to (A.6) we can then, for our present purposes, effectively ignore the remaining  $k_i$  dependence of the quark loop (including the propagators that we ignored in the above discussion). If we parameterize  $q$  as

$$q = \left( q_0, q_{1-}, q_{2-}, q_{3-} \right) \quad (4.6)$$

we can treat the  $q_{i-}$  as independent variables, with  $q_0$  essentially determined by the constraint  $q^2 \sim 0$ . The logarithmic cuts of (4.2) and (4.4) appear, respectively, in the  $q_{1-}$  and  $q_{2-}$  planes and if we make a further change of variables to

$$q_{1-} = x_2 x_3, \quad q_{2-} = x_3 x_1, \quad q_{3-} = x_1 x_2 \quad (4.7)$$

the two branch points appear in the  $x_3$ -plane, for fixed, positive,  $x_1, x_2$ , as illustrated in Fig. 4.3(a).



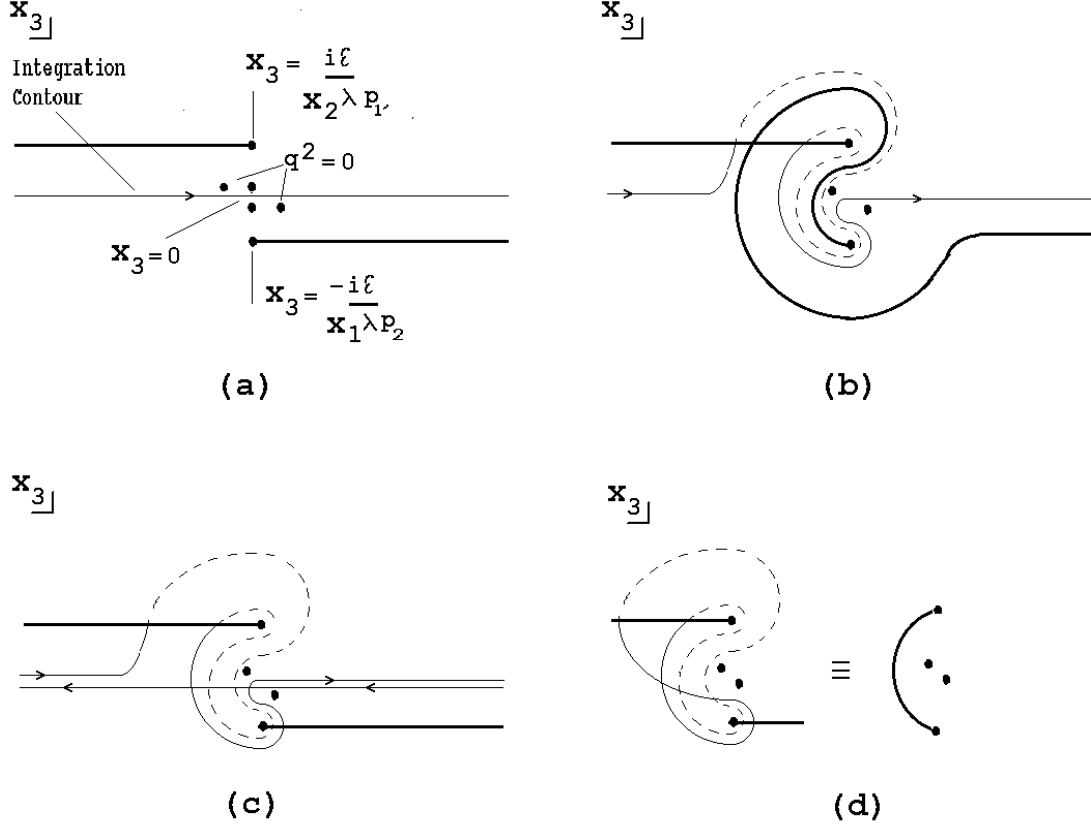


Fig. 4.3 Contours in the  $x_3$ -plane (a) the initial contour (b)  $p_2 \rightarrow e^{2\pi i} p_2$  (c) the discontinuity (d) the discontinuity as a line integral.

(The branch points also appear, separately, in the  $x_2$  and  $x_1$  planes. To focus on the  $s_{1/2}$  discontinuity and avoid any complication from discontinuities involving a logarithm of  $p_3$  in these planes we can take the  $\lambda$  for this logarithm to be much smaller.) The propagator poles that are not on-shell, that we ignored in the above discussion, combine to give a multiple pole at  $q^2 = 0$  (on both sides of the contour, as determined by the presence of  $i\epsilon$  in all propagators). If we continue to ignore propagator numerators then the factors of  $1/q_{1-}$  and  $1/q_{2-}$ , in (4.2) and (4.4) respectively, will also contribute poles at  $x_3 = 0$  (that will partly be compensated by the jacobian due to the change of variables). However, in the anomaly contribution we will ultimately consider, these poles will be directly canceled by numerator factors.

The threshold we are interested in occurs when the two branch points collide (at  $x_3 = 0$  for  $\epsilon = 0$ ). To extract the discontinuity we consider a full-plane rotation of  $p_2$ , with  $p_{1'}$  fixed, so that the logarithmic branch-cut (4.4) deforms the contour as shown in Fig. 4.3(b) - the dashed line indicates that the contour is on the second sheet of the branch-point (4.2). (In this figure we have omitted the poles at  $x_3 = 0$ .) Note that the continuation path we have chosen isolates the discontinuity around the  $s_{1/2}$

branch cut, since it avoids the pinching of the integration contour with the singularity at  $q^2 = 0$  that would give other discontinuities. The desired discontinuity is obtained by adding the original contour in the opposite direction, as shown in Fig. 4.3(c). Combining both contours we obtain Fig. 4.3(d) which, as illustrated, can be written as a line integral between the two branch points of the double-discontinuity due to both cuts. As  $\epsilon \rightarrow 0$ , or in the asymptotic limit  $p_{1'}, p_2 \rightarrow \infty$ , the branch points approach each other and the result is a closed contour integral around the singularity at  $q^2 = 0$  which is independent of the position of the end points and remains finite in the asymptotic limit. This is the asymptotic discontinuity and the singularity at  $q^2 = 0$  is clearly crucial in producing a non-zero result.

In Fig. 4.4(a) we have illustrated the last stage of the contour contraction as  $\epsilon \rightarrow 0$  and have also included the effect of adding (external and internal) transverse momenta in the foregoing analysis. The integral between the branch points, of the double discontinuity, is still obtained, while the singularity at  $q^2 = 0$  separates into a set of poles at both positive and negative  $x_3$ .

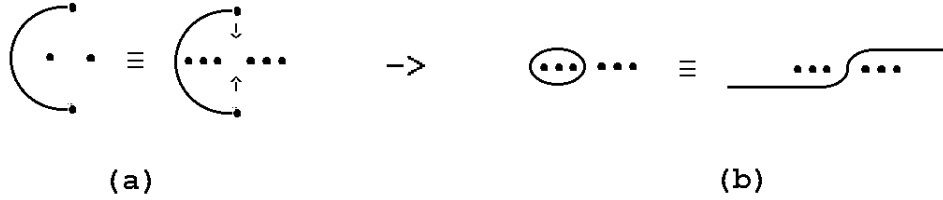


Fig. 4.4 (a) The  $x_3$  contour with finite transverse momenta (b) equivalence of the asymptotic contour to the original contour.

In Fig. 4.4(b) we have shown the asymptotic discontinuity. Since the branch points are logarithmic, the double discontinuity involved is simply  $4\pi^2$  and so no longer contains either branch cut. Consequently, the asymptotically finite integral around the poles to the left can be opened up to give the original contour, as illustrated. (If there is a singularity at  $x_3 = 0$ , the contour is constrained to pass through this point although, as we noted above, for the anomaly contribution to graphs, this will not be the case). The final result shown in Fig. 4.4(b) is just what would be given by the normal cutting rules for a discontinuity in  $s_{1'2}$ , i.e. the original integral with the four propagators involved in generating the discontinuity placed on-shell. Note that the same result is obtained if the discontinuity is evaluated by varying  $p_{1'}$ . An integral around the positive  $x_3$  poles appears at the intermediate stage, which can then be opened up to give the same final contour as in Fig. 4.4(b).

An obvious, but essential, requirement in the origin of the asymptotic discontinuity, which we want to emphasize, is that the branch-cuts due to the logarithms in  $p_{1'}$  and  $p_2$  must lie on opposite sides of the  $x_3$  contour. (This is the sign differ-

ence between (4.2) and (4.4) that we emphasized above.) In a physical region this requirement is normally straightforward for a loop integration producing a threshold due to two massive states since the loop momentum will flow oppositely through the two states and the  $i\epsilon$  prescription will place the states on opposite sides of the energy integration contour. In the variables we are using the generation of the threshold is a little more subtle. Note, for example, that when  $x_1 < 0$  the branch-point (4.2) appears in the upper half-plane (moving through infinity as  $x_1$  moves through zero) and there is no discontinuity. Therefore, the signs of the  $x_i$  play an essential role in the occurrence of the discontinuity. A further requirement, which clearly holds in the case just discussed, is that the trapping (pinching) of the contour that we have discussed must combine with the pinching associated with the logarithms to give a complete cut through the diagram. That is to say, the complete set of pinchings must correspond to an overall invariant cut.

## 4.2 Maximally Non-Planar Unphysical Discontinuities

We consider next the unphysical discontinuities that are our principal interest. According to the discussion in Section 3, we are looking for a triple discontinuity of the form of Fig. 3.5 that treats the three cut lines of the quark loop symmetrically so that, in a physical region, the sign of the energy component can be the same for all three on-shell states. We will, therefore, confine our discussion to a search for a symmetric triple discontinuity. As we noted, if the normal cutting rules apply there is no triple discontinuity (symmetric or not) of the Fig. 3.5 kind. We consider whether the direct evaluation of discontinuities gives the same result.

The discontinuity we discussed above occurred in a physical region that is unsymmetric in that  $P_2$  is the momentum of an incoming particle while  $P_1$  is the momentum of an outgoing particle. To look for a symmetric discontinuity we will use an analysis that treats the complete graph symmetrically throughout. To this end, we start in the symmetric asymptotic region (3.1) where all momenta are real and

$$s_{ij} \sim -p_i p_j < 0 \quad (4.8)$$

In this region, the diagram is defined by the usual  $i\epsilon$  prescription. Since all three invariants must be positive, the triple discontinuity of Fig. 3.5 can only be present in the triple-regge limit if we allow the large momenta involved to be unphysical. A symmetric way to do this is to start from the real physical region and take

$$p_i \rightarrow e^{-i\pi/2} p_i = ip_i, \quad i = 1, 2, 3 \quad \Rightarrow s_{ij} \sim (-ip_i)(ip_j) > 0 \quad (4.9)$$

Given the symmetry of the present discussion, it is immediately apparent that there will not be a (symmetric) triple discontinuity, as we now argue. Using the above analysis, logarithms will be generated by each of the  $k_i$  integrations. If we consider again the region where the transverse momenta are close to zero then, from (A.6),

the requirement that the energy component of each on-shell line in the loop have the same sign is equivalent to requiring that the  $q_i$ - all have the same sign. This, in turn, requires that the  $x_i$  should all have the same sign. However, in the symmetric real physical region, if  $x_1$  and  $x_2$  have the same sign, the logarithmic branch cuts in  $P_1$  and  $P_2$  lie on the same side of the  $x_3$  contour as illustrated in Fig. 4.5.

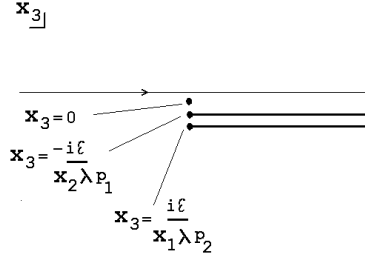


Fig. 4.5 The Symmetric Location of Branch-Cuts in the  $x_3$ -plane.

Since the continuation (4.9) is symmetric they will remain on the same side after the continuation. As a consequence, in the symmetric  $x_i$  region, the contour will not be trapped and distorted as one branch point moves around the other, as it was in Fig. 4.3, and no discontinuity will result. We conclude therefore that, for the graph we are discussing, discontinuities can only be generated in asymmetric regions of the  $x_i$  that can not provide the symmetric triple discontinuity that we are looking for. The foregoing analysis also precludes the occurrence of a triple discontinuity, that is appropriately symmetric, in the diagram of Fig. 3.6.

### 4.3 A Symmetric Unphysical Triple Discontinuity

To obtain a symmetric triple discontinuity we look for a graph that has the appropriate overall symmetry and also, for each  $i \neq j \neq k$ , has logarithmic branch cuts on both sides of the  $x_i$  contour in a symmetric region of  $x_j$  and  $x_k$ . With these requirements in mind, an obvious graph to consider is that of Fig. 3.7. To discuss this graph we continue, for simplicity, to take  $Q_1 = Q_2 = Q_3 = 0$ . Two symmetric (distinct) routes for the internal momenta are shown in Fig. 4.6. To be consistent with our previous notation we have used the notation that we direct the  $k_i$  momenta in the opposite direction to the  $P_i$ ,  $k'_i$  momenta in the opposite direction to the  $P'_i$  (i.e. in the same direction as the  $P_i$ ) and direct the internal loop momentum in the same direction as the  $k'_i$  momenta.

For a threshold corresponding to the cutting of particular lines of the internal quark loop to be generated the external loop momentum generating the relevant logarithms must pass through at least one of the lines. With this constraint, only the routing shown in Fig. 4.6(a) will give both discontinuities of the kind we are looking for and the  $\gamma$ -matrix structure for on-shell contributions that we show, in the next Section, gives the anomaly. The routing of Fig. 4.6(b) would be appropriate for

discussing the triple discontinuity of Fig. 3.7(b). However, as we noted in the previous Section, and will explain further below, this triple discontinuity does not contain the symmetric momentum configuration needed for the anomaly.

Using the momentum routing of Fig. 4.6(a) we consider the logarithms generated by both the  $k_i$  and  $k'_i$  loop integrations. Extracting all logarithms places on-shell all the hatched lines of Fig. 4.6(a), and gives leading behavior of the form of (3.2) multiplied by double logarithms of each of the  $P_{i+}$ .

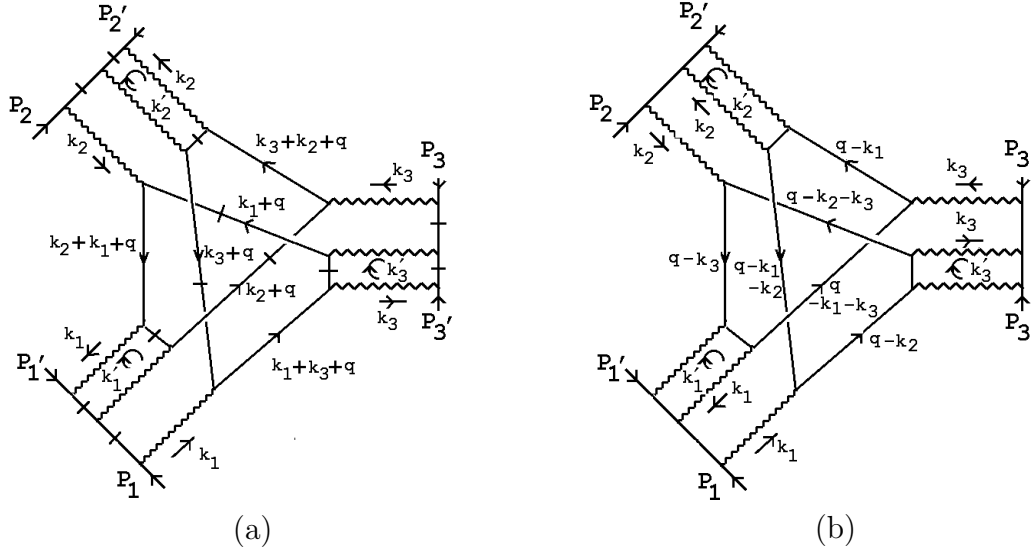


Fig. 4.6 Labeling Momenta for Fig. 3.7(a).

How the logarithms cancel or combine with other diagrams is, of course, a very complicated problem. As we have emphasized, to discuss this systematically we must consider all the multiple asymptotic discontinuities that occur rather than the behavior of full diagrams. Our present concern is, however, the much narrower purpose of determining only whether there is a symmetric triple discontinuity in which the anomaly can occur.

As above, to study discontinuities we keep the  $q$ -dependence of all logarithms together with all  $i\epsilon$  dependence. We consider specifically the logarithms generated by the  $k_1$  and  $k'_1$  loops, but the symmetry of the diagram obviously determines that the others can be treated identically. The loops, extracted from Fig. 4.6, are shown in Fig. 4.7. The  $k_1$  loop is identical to those of Fig. 4.2 and can be evaluated analogously.

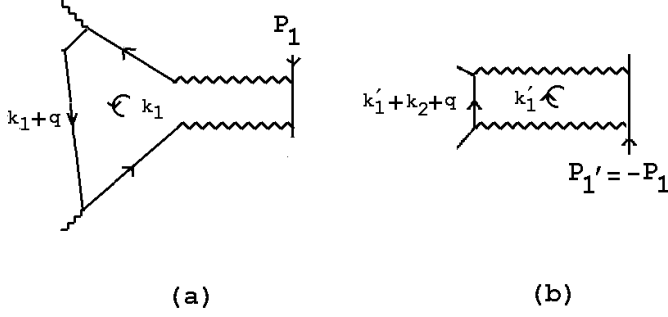


Fig. 4.7 (a) The  $k_1$  Loop (b) The  $k'_1$  Loop.

Using a similar analysis, the  $k'_1$  loop gives an integral of the form

$$\int_0^{(k_2+q)_{1-}} dk'_{11-} \dots \quad (4.10)$$

If we again go to the region where all transverse momenta are close to zero then, We have drawn the diagrams as basic anomaly processes in Fig. 6.1 using (A.6), it follows that after the  $k_2$  integration

$$k_{21-} \sim k_{20} \sim q^2/q_{2-} \ll q_{1-} \quad (4.11)$$

Therefore, we can take the upper end-point in (4.10) to be  $q_{1-}$ . In this case both the  $k_1$  and  $k'_1$  integrations give logarithms with  $q_{1-}$  in the argument - but with opposite signs. We then have branch-cuts located as in Fig. 4.8(a) in each of the  $x_1, x_2$  and  $x_3$  planes.

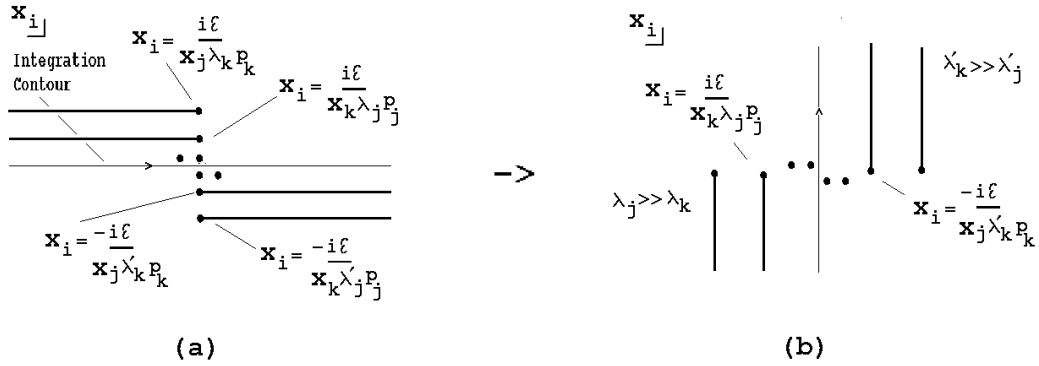


Fig. 4.8 (a) Branch Points in the  $x_i$ -plane (b)  $p_i \rightarrow e^{-i\pi/2}p_i = ip_i$ ,  $i = 1, 2, 3$

We have included the poles at  $q^2 = 0$  and  $x_i = 0$  and have used different  $\lambda_i$  and  $\lambda'_i$  for each branch-cut to allow us to separate the branch points in our discussion.

With values of the  $\lambda_i$  and  $\lambda'_i$  implied by Fig. 4.8(a), we could clearly obtain a discontinuity in  $s_{jk'}$  (due to the two closest branch points) by repeating the discussion

illustrated by Fig. 4.3. The discontinuity would similarly be an integral between the two branch points involved, as in Fig. 4.3(d), but because of the additional branch points that are present, the contour could not be opened up as in Fig. 4.4. Therefore, having taken  $x_j, x_k > 0$  so that the branch cuts lie as in Fig. 4.8(a), the discontinuity would involve only pure imaginary or negative real part values of  $x_i$ . Consequently, any further discontinuity obtained by the collision of branch points in the  $x_j$  or  $x_k$  planes would have to involve mixed real part signs for the  $x_i$ . We conclude (not surprisingly) that in the physical region a triple discontinuity can not be obtained that involves only positive values of all three  $x_i$ .

This brings us to the central point of the paper. If we go to the unphysical region (4.9), where we expect to encounter an unphysical triple discontinuity, the last analysis changes in a crucial manner. The resulting location of branch cuts is now as shown in Fig. 4.8(b), allowing the integration contour to be rotated as illustrated. In Fig. 4.8(b) we have also, for emphasis, chosen significantly different values of the  $\lambda_i$  and  $\lambda'_i$ . If we again determine the discontinuity associated with the collision of the two nearest branch points, as above, the result will be the contour integral of the double discontinuity shown in Fig. 4.9.

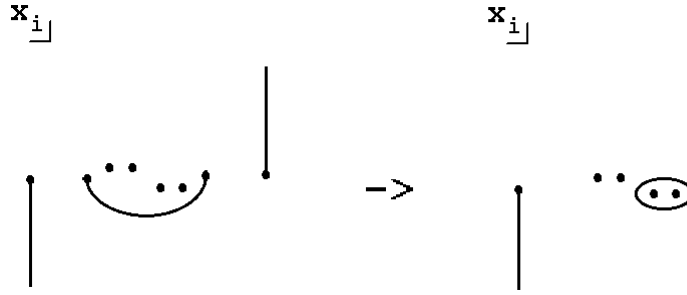


Fig. 4.9 The unphysical region discontinuity.

Now the integral involves positive real values of  $x_i$  and, as illustrated, the asymptotic limit gives a loop integral over just positive values. The contour integral can not be opened up, however, since the other branch cuts remain.

Having derived a first discontinuity from two branch points in the  $x_i$  plane, as in Fig. 4.9, it is straightforward to keep the remaining branch points and move on to the  $x_j$  and  $x_k$  planes where, in each case, only two branch cuts now appear. In both planes, discontinuities of the form of Fig. 4.9 occur, provided the  $x_i$  integration is restricted to positive real values. Therefore, we obtain a triple discontinuity in which each of the  $x_i$ ,  $x_j$  and  $x_k$  integrations is consistently over positive values and the asymptotic contour is obtained as illustrated by the first two contours in Fig. 4.10.



Fig. 4.10 Contours for the  $x_i$ ,  $x_j$  and  $x_k$  integrations.

Since all logarithmic branch cuts are now removed, all three contours can be opened up to obtain the last contour of Fig. 4.10 which is, once again the original contour of integration for each of  $x_i$ ,  $x_j$  and  $x_k$ . We thus obtain a triple discontinuity which, at first sight, corresponds to the usual cutting rules since all cut lines are on-shell. However, the triple discontinuity is truly symmetric and as a result each discontinuity is, necessarily, a pseudothreshold. There is also a very important further subtlety.

If we consider the discontinuity arising from the pinching of logarithms of  $p_1 \lambda_1$  and  $p_2 \lambda'_2$ , for example, then the lines put on-shell in the discontinuity are those that have thick hatches in Fig. 4.11(a).

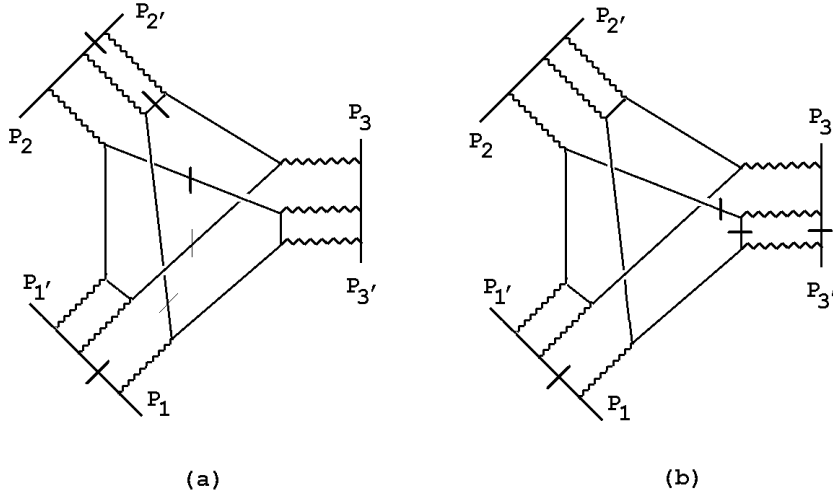


Fig. 4.11 On-shell lines for (a) an  $s_{12'}$  discontinuity (b) a potential  $s_{13'}$  discontinuity.

These lines are only a subset of those required to obtain a complete cut of the diagram. This implies that the corresponding pinching does not, by itself, give a singularity of the complete integral and a-priori the integration contour could be deformed away from the pinched region. To obtain a complete cut we must add the lines that have thin hatches in Fig. 4.11(a). When these lines are on shell the pinching does give an overall singularity. But, if we require a common sign for the  $x_i$  the two thin-hatched lines again have the wrong momentum direction to straightforwardly combine with the asymptotic pinching to give what would be a physical sheet “asymptotic normal



threshold”. However, each of the two thin hatched lines is separately placed on shell by one of the additional discontinuities. Therefore, the full triple discontinuity we have found does correspond to a triplet  $\{s_{12'}, s_{23'}, s_{32'}\}$  of invariant (pseudothreshold) cuts.

If we consider instead the discontinuity arising from the pinching of logarithms of  $p_1\lambda_1$  and  $p_3\lambda_3'$  then the lines put on shell are those hatched in Fig. 4.11(b). In this case there is no simple way to include additional lines and obtain an invariant cut. Therefore, this pinching can not be extended to a complete cut of the diagram. We conclude that the triple discontinuity in  $\{s_{12'}, s_{23'}, s_{32'}\}$  that is illustrated in Fig. 3.8 is the only combination that exists, as an extension of the above analysis. It is symmetric, with each of the internal quark lines that are put on shell by  $k_i$  integrations treated symmetrically. All three of these lines contribute to each invariant cut but, as we have just discussed, two of them always have the wrong  $i\epsilon$  prescription, relative to the third, to give a physical normal threshold. Singularities associated with combinations of forward and backward going particles are “mixed- $\alpha$ ” solutions of the Landau equations[16]. In general, such “pseudothresholds” are not singular on the physical sheet because of the conflicting  $i\epsilon$  prescriptions. However, they are generally singular on unphysical sheets and can appear in multiple discontinuities. They would be particularly expected to appear in unphysical multiple discontinuities.

Finally, we return to the triple discontinuity of Fig. 3.7(b), using the momentum routing of Fig. 4.6(b). Consider, for example, the discontinuity in  $s_{2'3}$ . This will be due to the pinching of the  $x_1$  integration contour by the logarithms generated from the  $k_2'$  and  $k_3$  integrations. The relevant sub-part of Fig. 4.6(b) is shown in Fig. 4.12.

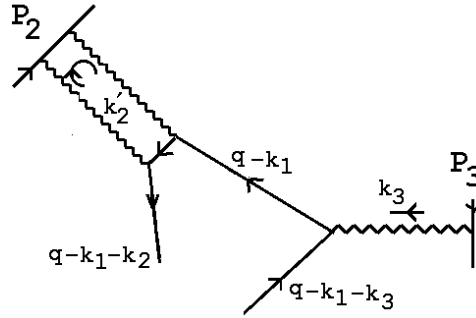


Fig. 4.12 Part of the  $q$  momentum flow within Fig. 4.6(b)

That the direction of the  $q$ -momentum flow is opposite, relative to  $k_2'$  and  $k_3$ , along the relevant internal lines implies that  $x_2$  and  $x_3$  must have opposite signs in order for the branch cuts to be on opposite sides of the  $x_1$  contour. As a result no symmetric triple discontinuity exists.

There are clearly two criteria for the existence of a symmetric asymptotic triple

discontinuity - that we will appeal to further in the next Section. The first is that the  $q$  momentum flow must be in the same relative direction along the relevant internal lines for each discontinuity. The second is that all internal loop lines, besides those in the remaining triangle, must be put on shell by the combination of the three pinches of the  $x_i$  integrations.

## 5. THE TRIANGLE ANOMALY AND OTHER DIAGRAMS

In this Section we discuss how the anomaly occurs in a reggeon vertex obtained from the triple discontinuity of Fig. 3.8. We will also consider other diagrams that can contribute and discuss how color quantum numbers determine which reggeon interactions are involved.

### 5.1 The Asymptotic Amplitude

We can briefly describe the calculation of the asymptotic amplitude obtained from Fig. 3.8 (in which all the cut lines are put on-shell as described in the last Section) as follows. Additional background description of the method used can be found in [10]. We begin by adding in the numerator dependence that we essentially ignored in the previous Section. For the external lines, additional powers of the external momenta are generated as in (A.9) and (A.10). As a result, inverse external momentum factors, such as  $p_1'^{-1}$  in (4.2) and  $p_2^{-1}$  in (4.4) are eliminated and the factor of  $P_1+P_2+P_3$  that appears in (3.2) is produced. Also, if we use the natural transverse momenta given by (4.3), the light-like  $\gamma$ -matrix couplings that appear at each of the vertices of the internal loop (after the triple-regge limit is taken) are as illustrated in Fig. 5.1(a).

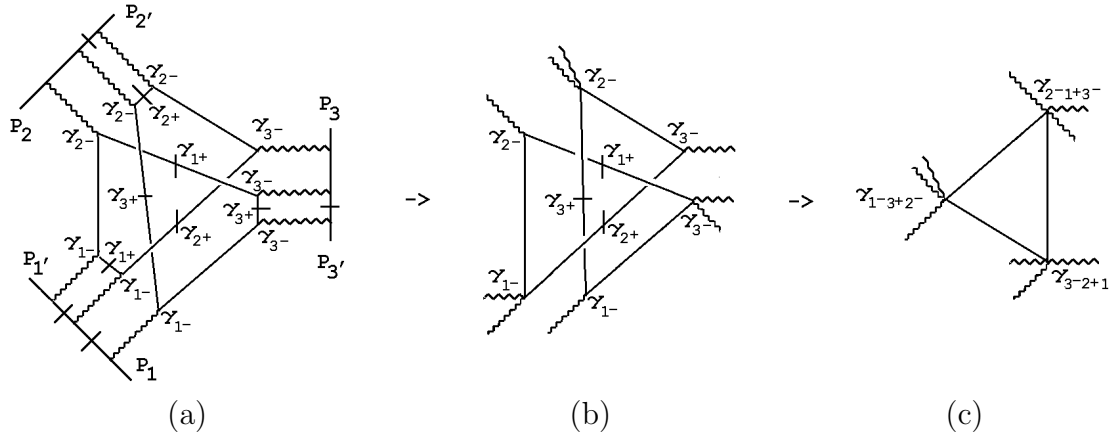


Fig. 5.1  $\gamma$ -matrix structure for the reggeon interaction extracted from Fig. 3.7.

For the hatched lines that appear in both Fig. 5.1(a) and (b), we keep the  $\gamma$  matrices shown. These are the “local couplings” (see [10]) that appear when that part of the associated numerator is kept that cancels the internal momentum factors that arise from the longitudinal loop momentum integrations (such as  $q_{1-}^{-1}$  in (4.2) and  $q_{2-}^{-1}$  in

(4.4) ). To justify this procedure we appeal to the (“infra-red non-renormalization”) argument of Coleman and Grossman[17] that only a fermion triangle diagram, with particular helicities for the couplings, can produce the anomaly infra-red divergence.

We introduce external transverse momenta (that we essentially ignored in the previous Section) using the notation illustrated in Fig. 5.2(a).

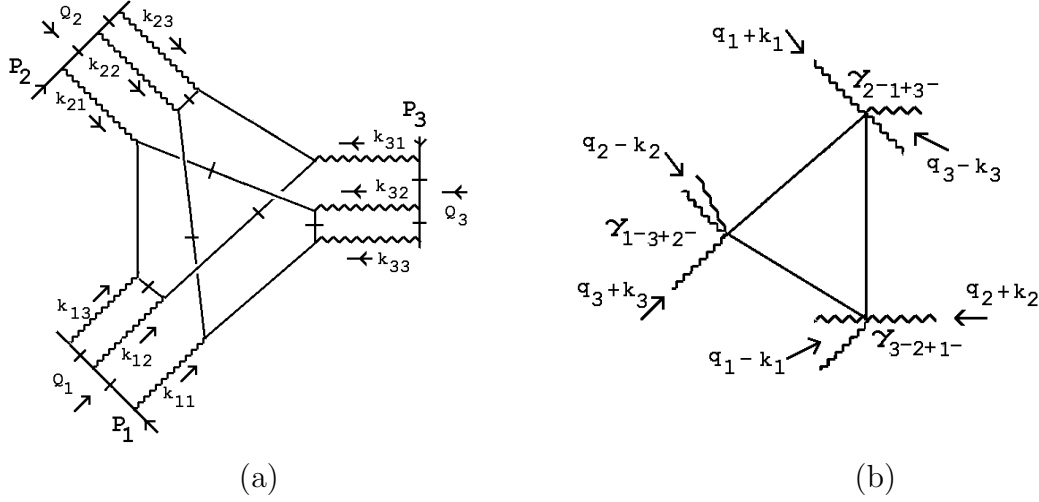


Fig. 5.2 (a) Notation for (5.1) (b) Notation for (5.4)

The resulting asymptotic behavior then has the form

$$P_{1+} P_{2+} P_{3+} \prod_{i=1}^3 \int \frac{d^2 k_{i1} d^2 k_{i2} d^2 k_{i3}}{k_{i1}^2 k_{i2}^2 k_{i3}^2} \delta^2(Q_{i\perp} - k_{i1} - k_{i2} - k_{i3}) G_i^3(k_{i1}, k_{i2}, k_{i3} \dots) \times R^9(Q_1, Q_2, Q_3, k_{11}, k_{12}, k_{13} \dots) \quad (5.1)$$

where  $R^9$  is the triangle diagram illustrated in Fig. 5.1(c). Note that this diagram depends only on  $k_{i2} + k_{i3}$  (i.e. it is independent of  $k_{i2} - k_{i3}$ ).

## 5.2 The Reggeon interaction Anomaly

By comparing with the generalization[10] of (3.6) and (3.7) to three reggeons in each  $t$ -channel, we can directly interpret  $R^9$  as a nine-reggeon interaction. If we write

$$k_{i1} = q_i + k_i, \quad k_{i2} = (q_i - k_i)/2 - k'_i, \quad k_{i3} = (q_i - k_i)/2 + k'_i, \quad (5.2)$$

then the momentum flow into the triangle diagram of Fig. 5.1(c) is as shown in Fig. 5.2(b). Using momentum conservation, i.e.

$$q_1 + q_2 + q_3 = 0 \quad (5.3)$$

$R^9$ , which does not depend on the  $k'_i$ , can be written (very similarly to (3.4)) as

$$R^9(q_1, q_2, q_3, k_1, k_2, k_3) = \int d^4k Tr\{\gamma_5 \gamma^{1^-3^+2^-} (\not{k} + \not{k}_2 + \not{q}_3 - \not{k}_1) \frac{\gamma_5 \gamma^{2^-1^+3^-} (\not{k} - \not{q}_2 + \not{q}_3 - \not{k}_2 - \not{k}_3) \gamma_5 \gamma^{3^-2^+1^-} (\not{k} + \not{k}_1 - \not{q}_2 - \not{k}_3)}{(k + k_2 + q_3 - k_1)^2 (k - q_2 + q_3 - k_2 - k_3)^2 (k + k_1 - q_2 - k_3)^2}\} \quad (5.4)$$

where

$$\begin{aligned} \gamma^{1^-3^+2^-} &= \gamma_{1^-} \gamma_{3^+} \gamma_{2^-} = \gamma^{-,-,-} - i \gamma^{-,-,+} \gamma_5 \\ \gamma^{2^-1^+3^-} &= \gamma_{2^-} \gamma_{1^+} \gamma_{3^-} = \gamma^{-,-,-} - i \gamma^{+,-,-} \gamma_5 \\ \gamma^{3^-2^+1^-} &= \gamma_{3^-} \gamma_{2^+} \gamma_{1^-} = \gamma^{-,-,-} - i \gamma^{-,+, -} \gamma_5 \end{aligned} \quad (5.5)$$

and  $\gamma^{\pm,\pm,\pm}$  is defined by (3.5). Again we obtain a particular component of the tensor that describes the triangle diagram contribution to a three current vertex function, i.e. we can write

$$\begin{aligned} R^9(q_1, q_2, q_3, k_1, k_2, k_3) &= (n_{\mu}^{-,-,-} - i n_{\mu}^{-,-,+})(n_{\alpha}^{-,-,-} - i n_{\alpha}^{+,-,-})(n_{\beta}^{-,-,-} - i n_{\beta}^{-,+, -}) \\ &\quad \times T^{\mu\alpha\beta}(k_1 - k_3 - q_2, k_2 - k_1 - q_3) \end{aligned} \quad (5.6)$$

where  $T^{\mu\alpha\beta}$  is the triangle diagram three current amplitude.

To discuss the occurrence of the anomaly in (5.5) we first recall the general invariant decomposition of  $T_{\mu\alpha\beta}$  as discussed in [6]. With the notation illustrated in Fig. 5.3

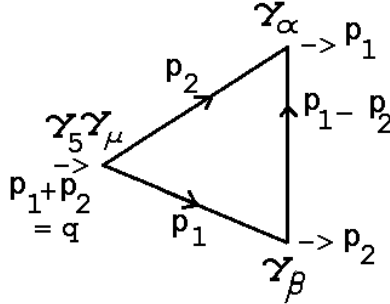


Fig. 5.3 Triangle Diagram Notation

we can write

$$\begin{aligned} T_{\mu\alpha\beta}(p_1, p_2) &= A_1 \epsilon_{\sigma\alpha\beta\mu} p_1^{\sigma} + A_2 \epsilon_{\sigma\alpha\beta\mu} p_2^{\sigma} + A_3 \epsilon_{\delta\sigma\alpha\mu} p_{1\beta} p_1^{\delta} p_2^{\sigma} \\ &\quad + A_4 \epsilon_{\delta\sigma\alpha\mu} p_{2\beta} p_1^{\delta} p_2^{\sigma} + A_5 \epsilon_{\delta\sigma\beta\mu} p_{1\alpha} p_1^{\delta} p_2^{\sigma} + A_6 \epsilon_{\delta\sigma\beta\mu} p_{2\alpha} p_1^{\delta} p_2^{\sigma} \end{aligned} \quad (5.7)$$

The ultra-violet anomaly occurs in the first two terms of (5.7), i.e.

$$T_{\mu\alpha\beta}(k_1, k_2) = \frac{1}{4\pi^2} \epsilon_{\sigma\alpha\beta\mu} p_1^\sigma + \frac{1}{4\pi^2} \epsilon_{\sigma\alpha\beta\mu} p_2^\sigma + \dots \quad (5.8)$$

leading to the well-known divergence equation

$$(p_1 + p_2)^\mu T_{\mu\alpha\beta} = \frac{1}{2\pi^2} \epsilon_{\delta\sigma\alpha\beta} p_1^\delta p_2^\sigma \quad (5.9)$$

The ultra-violet anomaly can therefore appear only in a tensor component with three orthogonal Lorentz indices. If we keep just the  $\gamma_5$  parts of the three vertices in (5.5) we obtain a non-zero projection on such a tensor component. In fact this contribution to  $R^9$  retains the full symmetry of the original feynman diagram of Fig. 3.7(a) and, as a result, has the necessary symmetry to contain the ultra-violet anomaly.

The infra-red “anomaly pole” occurs in  $A_3$  and  $A_6$ . When  $p_1^2 = 0$

$$A_3 = -A_6 = \frac{1}{2\pi^2} \frac{1}{p_2^2 - q^2} \left( \frac{p_2^2}{p_2^2 - q^2} \ln \frac{p_2^2}{q^2} - 1 \right) \quad (5.10)$$

and when  $p_2^2 \rightarrow 0$

$$A_3 \rightarrow \frac{1}{2\pi^2} \frac{1}{q^2} \quad (5.11)$$

That is, a pole appears in  $A_3$  ( $= -A_6$ ) and, as a consequence of all divergence equations, the coefficient is also given by the anomaly. If, instead, we integrate over spacelike values of  $q^2$ , we obtain

$$\int dq^2 A_3(q^2, p_2^2) f(q^2, p_2^2) \xrightarrow[k_2^2 \rightarrow 0]{} \frac{1}{\pi} f(0, 0) = \int dq^2 \frac{1}{\pi} \delta(q^2) f(q^2, 0) \quad (5.12)$$

(provided  $f(q^2, p_2^2)$  is regular at  $q^2, p_2^2 = 0$ ). As we discussed in [6], the pole (5.11) is responsible for the appearance of a Goldstone boson pole in amplitudes containing the chiral flavor anomaly. For the reggeized gluon interactions that we are discussing it is the  $\delta$ -function property that is important.

The tensor factors multiplying  $A_3$  and  $A_6$  in  $T_{\mu\alpha\beta}$  potentially suppress the  $q^2 \rightarrow 0$  divergence due to the anomaly pole. To describe this, we consider a specific momentum configuration, e.g.

$$\begin{aligned} p_1 &= (p/\sqrt{2}, p/\sqrt{2}, 0, 0) \\ p_2 &= (-p/\sqrt{2}, -p \cos \theta/\sqrt{2}, 0, -p \sin \theta/\sqrt{2}) \\ \theta \xrightarrow{\sim} 0 &- p_1 = (0, 0, p\theta/\sqrt{2}, 0) = -p_1 = (0, 0, q, 0) \end{aligned} \quad (5.13)$$

where

$$q^2 = (p_1 + p_2)^2 \underset{\theta \rightarrow 0}{\sim} \quad (5.14)$$

In this configuration, we obtain the largest numerator if we consider the anomaly contribution of  $A_3$  to, say,  $T_{--3}$ . This has the form

$$T_{--3} = \epsilon_{\sigma\delta-3} \frac{p_1^\sigma p_2^\delta p_{1-}}{q^2} = \frac{p^2[p\theta/\sqrt{2}]}{q^2} \underset{\theta \rightarrow 0}{\sim} \frac{\sqrt{2}p}{\theta} \quad (5.15)$$

and so the divergence is suppressed, but only partially. A divergence of the form (5.15) is the strongest that can be obtained.

In general, to obtain the maximal infra-red divergence we must have a component of  $T_{\mu\alpha\beta}$  with  $\mu = \alpha$  and with  $\mu$  having a light-like projection. The corresponding light-like momentum must also flow through the diagram.  $\beta$  must have an orthogonal spacelike projection and the transverse momentum that vanishes, as  $q^2 \rightarrow 0$ , must be in the remaining orthogonal spacelike direction. If we choose the  $\gamma_5$  component from all three vertices in (5.5) the first requirement is not met. However, if we choose the  $\gamma_5$  component from one vertex and choose the vector coupling from the other two vertices, it is met. The finite light-like momentum involved must then have a projection on  $n^-, -, -^\mu$  and the orthogonal spacelike momentum must be distinct in each case. There is then a divergence of the form of (5.15).

The three possibilities for the infra-red anomaly divergence to occur are associated with the three distinct hexagraphs described in [10], and hence with three distinct helicity amplitudes. In the analysis of [10] the co-ordinates used were asymmetric and were chosen to isolate one anomaly configuration. These co-ordinates were naturally associated with a particular hexagraph and the corresponding helicity amplitudes and limits. We could equally well use these co-ordinates in discussing Fig. 3.8. In which case, the  $\gamma_5$  and non- $\gamma_5$  components in two of the three  $\gamma$ -matrices in (5.5) are interchanged. The anomaly pole contribution then comes from the three  $\gamma_5$  components. In either case, the result is the same. We anticipate, but will not attempt to demonstrate here, that for each hexagraph amplitude the ultraviolet anomaly and anomaly pole components are related by reggeon Ward identities, just as corresponding components in (5.7) are related by normal vector Ward identities. (Note that the “ultraviolet” region for (5.4) is actually the region  $k \lesssim P_{1+} \sim P_{2+} \sim P_{3+}$ , rather than  $k \sim \infty$ .) This implies that the occurrence of the infra-red and ultra-violet anomalies in diagrams will be closely correlated. We will exploit this in the following.

As discussed at length in [10], while the triple discontinuity giving Fig. 5.1 occurs in an unphysical region, there will be a corresponding “real” reggeon interaction in physical regions. In particular, the anomaly infra-red divergence can occur in the physical-region configuration shown in Fig. 5.4. (The dots indicate that a

local interaction is involved.) The  $\gamma_5$  interaction is at the intermediate vertex and the light-like momenta are as in(3.10)-(3.14). Fig. 5.4 can then be identified with the basic anomaly process of Fig. 3.2 except that there is an additional wee gluon involved. There are also additional gluons with finite transverse momentum.

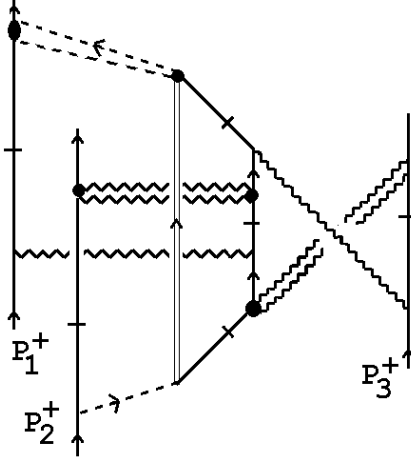


Fig. 5.4 A basic anomaly process associated with Fig. 5.1.

### 5.3 Other Diagrams

We now consider whether, based on the discontinuity analysis of the previous Section, there are other diagrams besides that of Fig. 3.7(a) that could contain the anomaly. We will not consider all possible diagrams - there are simply too many. We will make the simplifying assumption that only diagrams that are completely symmetric (with respect to the three  $t$ - channels) are relevant. There are two justifications for this assumption. First there is the infra-red light-cone argument discussed in Section 3. Secondly, we anticipate, as we have just discussed, that infra-red and ultraviolet anomalies should occur together so that reggeon Ward identities are satisfied. It seems that at this “simplest” level, where it first emerges, the ultraviolet anomaly is very likely to require a symmetric diagram.

If we begin from the diagram of Fig. 3.7(a) and retain only the exterior lines of the internal loop we obtain the “bare” diagram of Fig. 5.4(a). The exterior lines give the triangle diagram in the reggeon vertex. Since they must remain uncut when a triple discontinuity is taken they must remain on the exterior, as in the bare diagram. If we then add further lines such that a complete loop is formed within a symmetric diagram, and there is no sub-loop, the only new possibilities (up to reflections) are shown in Figs. 5.4(b)-(d).



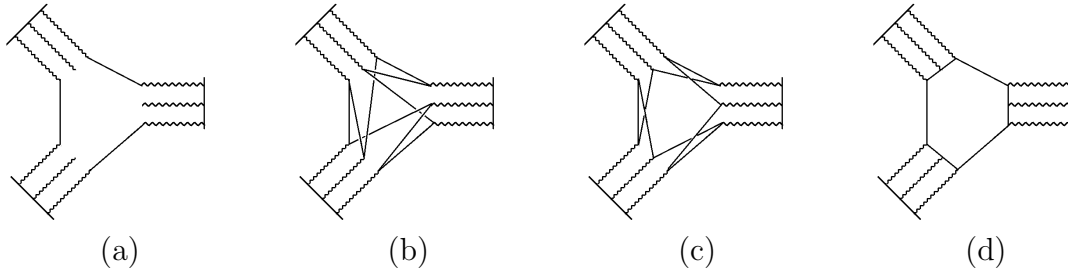


Fig. 5.4 (a) The “bare” diagram (b) - (d) Full diagrams.

The diagram of Fig. 5.4(b) can be analysed very similarly to our analysis of Fig. 3.7(a). As we described at the end of the last Section, a pseudothreshold triple discontinuity will be present if the six non-exterior loop lines can be grouped into three pairs, each associated with a particular discontinuity, such that the loop momentum flows across the discontinuity line in the same direction for each pair. In Fig. 5.5(a) we have drawn the appropriate cuts of Fig. 5.4(b) and in Fig. 5.5(b) we have isolated the cut lines that contribute to one discontinuity.

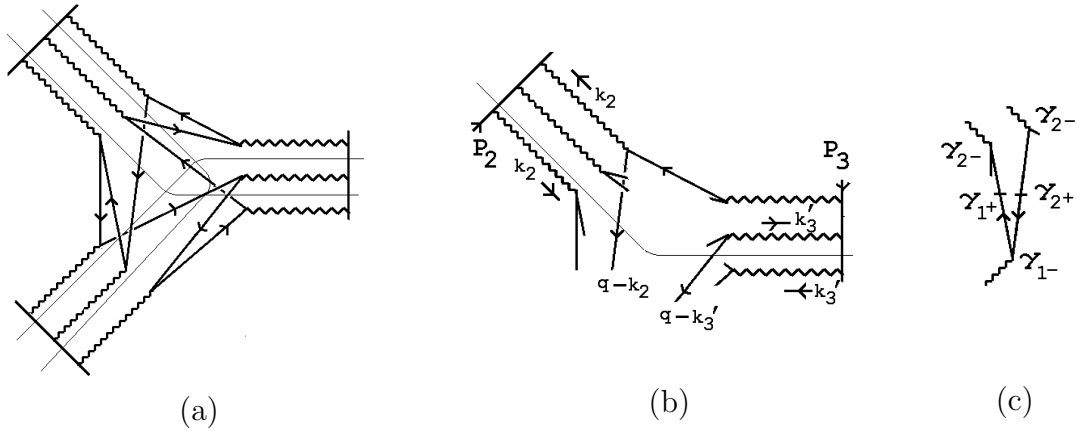


Fig. 5.5 (a) Cuts (b) one discontinuity (c) a  $\gamma$ -matrix vertex, of Fig. 5.3(b).

Both criteria for a symmetric triple discontinuity are satisfied. However, we must also consider the  $\gamma$ -matrix structure of the vertices that appear in the triangle diagram that is obtained. In fact, we find products of  $\gamma$ -matrices of the form shown in Fig. 5.5(c), which do not produce the  $\gamma_5$  coupling needed for the anomaly. The diagrams of Fig. 5.4(c) and (d) clearly do not have sufficient non-planar structure to give a pseudothreshold triple discontinuity. We conclude, therefore, that none of the additional diagrams of Fig. 5.4 can produce an anomaly contribution to a reggeon vertex.

## 5.4 Color Factors and Signature

Similarly to our discussion of the triple discontinuity of Fig.3.7(b), a priori  $R^9$  can contribute to vertices for fewer than nine reggeons. However, in [10] we argued that the anomaly would cancel, after all integrations over transverse momenta, unless each reggeon state has anomalous color parity (not equal to the signature). When SU(3) color amplitudes are obtained by first constructing the color superconducting theory with SU(2) color, as in [6], the relevant reggeon anomaly interactions are those for SU(2) reggeon states. In this case the simplest reggeon state with anomalous color parity is the color zero, odd signature, three reggeon state. A reggeon state that is “vector-like” in that it has (close to) unit angular momentum and appears in odd-signature amplitudes, is composed of (at least) three gluons, and has abnormal color parity, has all the quantum numbers of the anomaly current. As a result, the ultraviolet anomaly discussed above will directly involve interactions of the anomaly current. It is somewhat remarkable that we are led directly to the anomaly current by looking for the infra-red anomaly within reggeon interactions. For SU(3) color, a two reggeon even signature state with octet color and odd color parity would also be possible. For color zero, however, the three reggeon state is again the simplest possible.

If each reggeon state must contain at least three reggeons, the lowest-order reggeon vertex that can contain the anomaly is the nine reggeon vertex. In fact, we showed in [10] that the analyticity properties of amplitudes imply that the anomaly can only appear when signature conservation is also satisfied, which it is not if all three reggeon states carry odd signature. However, this conservation rule should be satisfied only after all relevant diagrams have been added. This would include the addition of all diagrams having the structure of Fig. 3.7(a) but with (one or two) incoming and outgoing lines interchanged. To avoid this cancelation additional reggeons (reggeized gluons or quarks) must be present. As we discuss in the next Section, additional reggeons are also required for the infra-red anomaly to play the dynamical role we anticipate.

Amplitudes giving vertices with four reggeons in each reggeon state no longer need to be completely symmetric, provided they collapse to give a symmetric triangle diagram. In fact, when four reggeons (or more) are present in each state a new subtlety arises in the process of taking a triple discontinuity. Consider the diagram shown in Fig. 5.6, which is a simple generalization of the diagram of Fig. 3.7(a) that we have discussed so much. Two of the single reggeon lines in Fig. 3.7(a) are replaced by two reggeons, with no additional non-planarity. In Fig. 5.6 we have also drawn triplets of cuts through the diagram in four distinct ways.

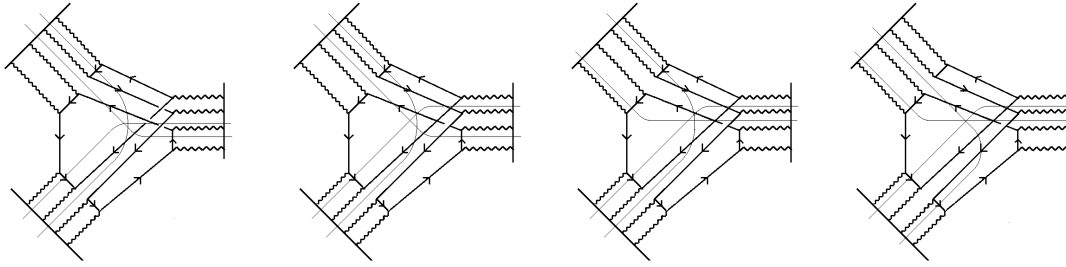


Fig. 5.6 Four triple cuts of a diagram for four reggeon states

These are the only possible triplets if we require pairs of non-exterior loop lines to be associated with each cut, such that the loop momentum flows across the cut line in the same direction for each pair. However, if we consider just one triplet and take asymptotic discontinuities for each cut (as above) by considering pairs of external logarithms, we do not obtain a complete triple discontinuity of the diagram. There are always three internal lines that are not put on shell. As a result, one or more, of the pinchings does not give a complete, invariant, cut of the diagram. To obtain a genuine triple discontinuity we have to combine all the pinchings of logarithms involved in the four sets of cuts shown in Fig. 5.6. All internal lines are then on shell and a complete triple discontinuity is obtained. The vertices for the corresponding triangle are the rotationally symmetric products of  $\gamma$ -matrices shown in Fig. 5.7 and so the extracted twelve reggeon vertex will contain the anomaly.

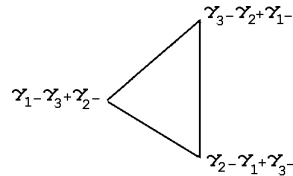


Fig. 5.7 The  $\gamma$ -matrix vertices obtained from Fig. 5.6

We will postpone a systematic discussion of cancelations, how and when the anomaly survives after all diagrams are summed etc., until following papers. Our priority in this paper has been simply to find diagrams in which an asymptotic discontinuity analysis determines that the anomaly is definitively present in the extracted reggeon interaction.

## 6. PION AND POMERON VERTICES IN COLOR SUPERCONDUCTING QCD

For completeness, we briefly describe the physical pomeron and pion interactions that appear in color superconducting QCD. Pion scattering is described in [6] and we anticipate that the corresponding multi-regge amplitudes are given by modifying the procedure described in [11] to incorporate the explicit structure of anomaly vertices that we have since discovered. Here we give only enough details to show that a straightforward extension of the above analysis will demonstrate that such interactions contain the anomaly.

When the  $SU(3)$  gauge symmetry of QCD is broken to  $SU(2)$  the infra-red divergence[6, 11] that involves the anomaly and that actually dominates bound-state interactions occurs in diagrams that are very similar to the ones we have discussed. The divergence is factorized off to give a wee-gluon condensate within both pion (i.e. Goldstone boson) bound states and the pomeron. The pomeron is a single reggeon (i.e. a massive,  $SU(2)$  singlet, reggeized gluon) within the wee-gluon condensate and the pion is a quark/antiquark pair in the same condensate. A diagram contributing to the triple-pomeron interaction is shown in Fig. 6.1(a) and a class of diagrams contributing to multipomeron interactions. is shown in Fig. 6.1(b).

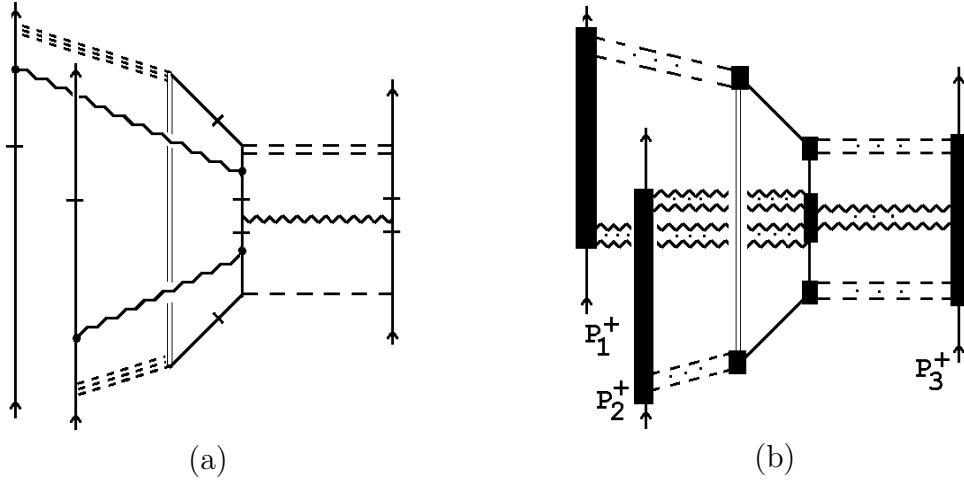


Fig. 6.1 (a) The triple pomeron interaction (b) A multipomeron interaction.

The scattering states are now pions and the solid, wavy, lines are reggeons. The dashed lines represent massless gluons that carry zero transverse momentum and, in collaboration with the anomaly, produce the divergence. The  $\delta$ -function due to

the anomaly produces transverse momentum conservation at the vertex where the reggeons interact.

We have drawn the diagrams as basic anomaly processes in Fig. 6.1, rather than in a form that exhibits their unphysical discontinuity properties. The triple pomeron process in Fig. 6.1(a) corresponds to a diagram that is just a little more complicated than the diagram of Fig. 5.6. There is an additional reggeon in each of the initial and final wee gluon configurations. The accompanying reggeon state contains two gluons - which can give the imaginary part of the single reggeon state that is anticipated to survive in the pomeron[6]. In both Fig. 6.1(a) and (b) the three multi-reggeon (pomeron) states that are interacting through the anomaly all have a wee-gluon component that participates in the divergence. In the notation of (3.10)-(3.14) the corresponding basic anomaly process involves (as already discussed in Section 3) taking the limit  $l \rightarrow 0$  while simultaneously making a boost  $a_z(\zeta)$  such that  $l \cosh \zeta = n$  is kept finite.

The diagram that gives the pion/pomeron coupling utilized in [6] is shown in Fig. 6.2(a). The corresponding basic anomaly process is shown in Fig. 6.2(b)

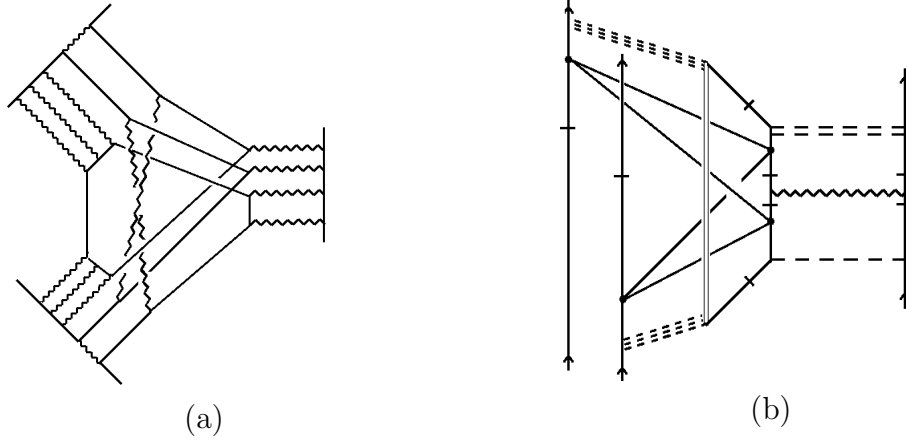


Fig. 6.2 The Pion/Pomeron Coupling (a) the feynman diagram (b) the basic anomaly process

The diagram of Fig. 6.2(a) has a triple discontinuity structure very similar to that of Fig. 5.6.

## APPENDIX: ASYMPTOTIC DISCONTINUITY ANALYSIS

In Section 4 we analyse triple-regge asymptotic discontinuities using a generalization of the simple light-cone analysis that we develop in the following.

Consider the box-diagram illustrated in Fig. A1.

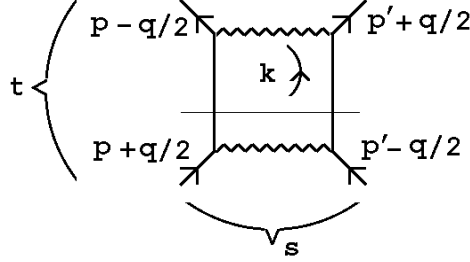


Fig. A1 The box diagram.

Initially we ignore the role played by numerators and so we consider, in the notation shown,

$$I(s, t, m^2) = \int d^4k \left[ k^2 - m^2 + i\epsilon \right]^{-1} \left[ \left( p - \frac{q}{2} + k \right)^2 - m^2 + i\epsilon \right]^{-1} \times \left[ (q - k)^2 - m^2 + i\epsilon \right]^{-1} \left[ \left( p' + \frac{q}{2} - k \right)^2 - m^2 + i\epsilon \right]^{-1}. \quad (A.1)$$

This integral is, of course, a function of invariants only even though it is specified using four momenta. Indeed, we can evaluate the integral using complex, unphysical, momenta that give physical values of the invariants, provided we are careful to define the integral via analytic continuation from the appropriate physical momentum region. Our purpose in this Section is to discuss momentum dependence of this kind for the simplifying case of the leading asymptotic behavior, in a manner that we apply to much more complicated diagrams in Section 4.

For illustrative purposes we set both  $q = 0$  and  $m = 0$  in (A.1) and ignore infra-red divergences. We can then write

$$I(s) = \int d^4k \left[ k^2 + i\epsilon \right]^{-2} \left[ (p + k)^2 + i\epsilon \right]^{-1} \left[ (p' - k)^2 + i\epsilon \right]^{-1} \quad (A.2)$$

We choose a particular Lorentz frame and introduce light-cone co-ordinates such that

$$p = \left( \frac{P_+}{2}, \frac{P_+}{2}, 0 \right) + O\left(\frac{1}{s}\right), \quad P_+ \sim s \rightarrow \infty$$

$$p' = \left( \frac{P'_+ + P'_-}{2}, \frac{P'_+ - P'_-}{2}, \underline{p}'_{\perp} \right) \quad (A.3)$$

so that  $s = P_+ P'_- [1 + O(1/s)]$ . We can then write

$$I(s) \underset{s \rightarrow \infty}{\sim} \frac{1}{2} \int d^2 \underline{k}_\perp dk_+ dk_- \left[ k_+ k_- - k_\perp^2 + i\epsilon \right]^{-2} \left[ (k_+ + P_+) k_- - \underline{k}_\perp^2 + i\epsilon \right]^{-1} \\ \times \left[ (k_+ - P'_+) (k_- - P'_-) - (\underline{k}_\perp - \underline{p}'_\perp)^2 + i\epsilon \right]^{-1} \quad (A.4)$$

To obtain a non-zero answer by closing the  $k_+$  contour, with  $k_-$  and  $k_\perp$  fixed, the three poles given by the three square brackets of (A.4) must not be on the same side of the contour. This requires  $0 < k_- < P'_-$  and, in this case, the  $k_+$  contour can be closed to pick up only the pole in the last bracket. This gives

$$k_+ = P'_+ + \frac{(\underline{k}_\perp - \underline{p}'_\perp)^2 - i\epsilon}{(k_- - P'_-)} \quad (A.5)$$

which is finite and so can be neglected compared to  $P_+$ . Note also that

$$k_- \sim 0, \quad k_\perp^2 \sim 0 \quad \Rightarrow \quad k_+ \sim 2k_0 \sim \frac{p'^2}{P'_-} \quad (A.6)$$

(we use this approximation in the analysis of Section 4). We thus obtain,

$$I(s) \underset{s \rightarrow \infty}{\sim} \pi i \int d^2 \underline{k}_\perp \left[ -k_\perp^2 + i\epsilon \right]^{-2} \int_0^{P'_-} dk_- \left[ k_- - P'_- \right]^{-1} \left[ P_+ k_- - \underline{k}_\perp^2 + i\epsilon \right]^{-1} \quad (A.7)$$

We are specifically interested in the leading real and imaginary parts of (A.7). They are given by the logarithm generated by the pole factor containing  $P_+$  as it approaches the  $k_- = 0$  end-point of the integration. If we keep only the integration over  $0 < k_- < \lambda P'_-$  and take  $\lambda \ll 1$  so that we can make the approximation  $k_-/P'_- \sim 0$  we obtain

$$I(s) \underset{s \rightarrow \infty}{\sim} \pi i \int d^2 \underline{k}_\perp \left[ -\underline{k}_\perp^2 + i\epsilon \right]^{-2} \frac{1}{P'_-} \int_0^{\lambda P'_-} dk_- \left( P_+ k_- - \underline{k}_\perp^2 + i\epsilon \right)^{-1} \\ \sim \frac{1}{P_+ P'_-} [\log (P_+ P'_- \lambda - \underline{k}_\perp^2 + i\epsilon)] J_1(0) \quad (A.8) \\ \sim \frac{1}{s} [\log (s\lambda + i\epsilon)] J_1(0) \sim \frac{1}{s} [\log s + i\pi] J_1(0)$$

where  $J_1(0) \sim \int d^2 \underline{k}_\perp \left[ -\underline{k}_\perp^2 + i\epsilon \right]^{-2}$  is infinite, but would be finite if we added a mass to the particle propagators.

As we have indicated, the sign of the imaginary part in (A.8) arises directly from the  $i\epsilon$  prescription. To obtain the leading imaginary part or, equivalently, the leading behavior of the discontinuity in  $s$ , it suffices to keep the  $i\epsilon$  dependence while dropping the  $-\underline{k}_\perp^2$  dependence in the  $k_-$  integral. (A.8) is, of course, independent of  $\lambda$ . It will, however, be useful to note the role of  $\lambda$  with respect to the analytic structure of  $I(s)$  in the  $s$ -plane. As illustrated in Fig. A2, the finite end of the branch-cut associated with the logarithm in (A.8) moves out as  $\lambda \rightarrow 0$ .

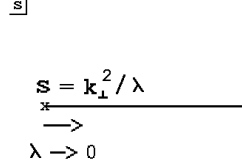


Fig. A2  $\lambda$ -dependence of the branch cut.

This is irrelevant to the asymptotic behavior and the “asymptotic discontinuity” clearly remains unchanged. We, nevertheless, exploit this simple feature in evaluating multiple discontinuities in Section 4. Also, although (A.8) is an invariant result, for our purposes it will be useful to keep the dependence on both  $P_+$  and  $P'_-$  and discuss the dependence of the phase on  $P_+$ .

The initial  $k_-$  integration contour for (A.8) is as shown in Fig. A3(a) with the pole at  $k_- = \underline{k}_\perp^2 / P_+$  indicated by a dot.

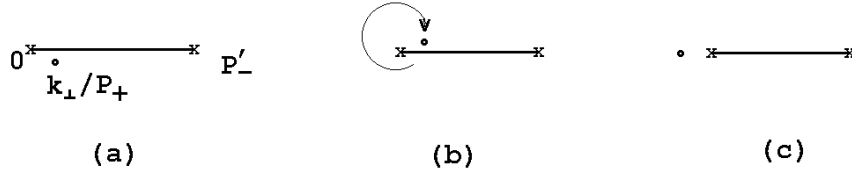


Fig. A3 Integration Contours for (a) (A.7) (b)  $P_+ \rightarrow e^{2\pi i} P_+$  (c) Fig. 4.4.

As  $P_+$  (and therefore  $s$ ) completes a circle in the complex plane the pole moves around the end-point as illustrated in Fig. A3(b). The result is that the phase of the logarithm in (A.8) changes from  $\pi$  to  $-\pi$  and there is a net discontinuity of  $2\pi i/s$ , as is given directly by (A.8). This is also the result that would be obtained by applying directly the standard cutting rules to Fig. A1, cut by the thin line, if the  $k_+$  and  $k_-$  integrations are used to put the vertical lines on shell. The above discussion is simply an asymptotic analysis of how the two cut propagators pinch the integration region to generate a branch-point in  $s$ . Introducing  $\lambda$  limits the integration region for the original integral such that the pinching only takes place for  $s \sim P_+ > 1/\lambda$ . Note also



that the residue function  $J_1(0)$ , multiplying the logarithm in (A.8), is directly obtained from the original box diagram by putting the cut lines giving the discontinuity on-shell using the longitudinal momentum integrations. This is a very simple example (the simplest) of the relationship between a discontinuity and asymptotic behavior.

In evaluating unphysical (multiple) discontinuities in Section 4 we do not assume that the standard cutting rules apply. Instead we directly analyse the discontinuities produced by logarithms. To understand how a discontinuity generated by a logarithm can provide leading asymptotic behavior we note that the twisted diagram of Fig. A4, for  $q = 0$ , differs from that of Fig. A1 only by  $P_+ \rightarrow -P_+$ .

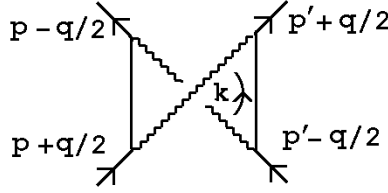


Fig. A4 The twisted box diagram.

As a result, the integration contour and pole position of Fig. A3(a) is replaced by that of Fig. A3(c). In this case a discontinuity is generated for  $s < 0$ . For  $s > 0$  there is no phase generated by Fig. A4 and only the real logarithms cancel when this diagram is added to that of Fig. A1. The leading behavior of the discontinuity in  $s$ , i.e the imaginary part, produced by the diagram of Fig. A1 remains. This cancelation of the logarithms is very well-known, of course. It is also well known that the cancelation fails when a non-abelian symmetry group is present and that a consequence is the reggeization of the gluon.

We can briefly summarize the effect of adding numerators to (A.1) as follows. First we note that the numerator of the internal fermion propagator carrying  $P_+$  gives an additional  $P_+$  factor of the form  $\gamma_- P_+$ . As a consequence, in (A.8), there is the replacement

$$\int_0 dk_- (P_+ k_- + \dots)^{-1} \rightarrow \gamma_- P_+ \int_0 dk_- (P_+ k_- + \dots)^{-1} \sim \log P_+ \quad (A.9)$$

and there is no inverse power of  $P_+$ . Also, each coupling to a gluon gives a  $\gamma$  matrix factor and since the external fermion lines are on-shell we can use the asymptotic form of the Dirac equation (i.e.  $\gamma_- P_+ \psi \sim m \psi$ ) to write

$$\begin{aligned} \langle P_+ | \gamma_\mu \gamma_- \gamma_\nu | P_+ \rangle &\sim \langle P_+ | \frac{\gamma_- P_+}{m} \gamma_\mu \gamma_- \gamma_\nu \frac{\gamma_- P_+}{m} | P_+ \rangle \\ &= \langle P_+ | P_+ \gamma_- P_+ | P_+ \rangle / m^2 \sim P_+ / m \end{aligned} \quad (A.10)$$

This gives another power of  $P_+$  ( $\sim s$ ) provided that the corresponding factor of  $P'_-$  is present in the finite momentum part of the scattering process. Not surprisingly this factor emerges from that part which would dominate if  $P'_-$  were large. However, we want to emphasize that this selection is made only by the need to form a Lorentz invariant amplitude from the non-invariant large momentum process.

Finally we note that the above analysis goes through with very little modification if we take both  $m^2$  and  $q$  to be non-zero so that (A.2) will not be infra-red divergent.

## References

- [1] V. N. Gribov, *Nucl. Phys.* **B139**, 1 (1978), G. 't Hooft, *Nucl. Phys. Proc. Suppl.* **B74**, 413 (1999).
- [2] M. F. Atiyah, in *Anomalies, Geometry and Topology*, edited by W. A. Bardeen and A. R. White (World Scientific, Singapore, 1985); R. Jackiw, *ibid.* and in *Effects of Dirac's Negative Energy Sea Quantum Numbers*, Dirac Prize lecture, March 1999, hep-th/9903255.
- [3] G. 't Hooft, *Phys. Rep.* **142**, 357 (1986).
- [4] D. Diakonov and V. Yu. Petrov, *Nucl. Phys.* **B272**, 457 (1986).
- [5] H. Leutwyler and A. Smilga, *Phys. Rev.* **D46**, 5607 (1992).
- [6] A. R. White, hep-ph/0202169.
- [7] E. A. Kuraev, L. N. Lipatov, V. S. Fadin, *Sov. Phys. JETP* **45**, 199 (1977); J. B. Bronzan and R. L. Sugar, *Phys. Rev.* **D17**, 585 (1978), this paper organizes into reggeon diagrams the results from H. Cheng and C. Y. Lo, *Phys. Rev.* **D13**, 1131 (1976), **D15**, 2959 (1977); V. S. Fadin and V. E. Sherman, *Sov. Phys. JETP* **45**, 861 (1978); V. S. Fadin and L. N. Lipatov, *Nucl. Phys.* **B477**, 767 (1996) and further references therein; J. Bartels, *Z. Phys.* **C60**, 471 (1993) and further references therein; A. R. White, *Int. J. Mod. Phys.* **A8**, 4755 (1993).
- [8] P. Goddard and A. R. White, *Nucl. Phys.* **B17**, 1, 45 (1970). As in [10] we emphasize that the full triple-regge limit is distinct from the “triple-regge” limit of the one-particle inclusive cross-section that is a “non-flip helicity-pole” limit.
- [9] A. R. White, *Phys. Rev.* **D29**, 1435 (1984).
- [10] A. R. White, *Phys. Rev.* **D63** 016007, (2001).
- [11] A. R. White, *Phys. Rev.* **D58**, 074008 (1998).
- [12] A. R. White, *Nucl. Phys. Proc. Suppl.* **96**, 277-286 (2001) - hep-ph/0008267; see also Lectures in the Proceedings of the Theory Institute on Deep-Inelastic Diffraction, Argonne National Laboratory (1998).
- [13] A. A. Migdal, A. M. Polyakov and K. A. Ter-Martirosyan, *Zh. Eksp. Teor. Fiz.* **67**, 84 (1974); H. D. I. Abarbanel and J. B. Bronzan, *Phys. Rev.* **D9**, 2397 (1974).
- [14] V. S. Fadin and L. N. Lipatov, *Nucl. Phys.* **B406**, 259 (1993).

- [15] O. Steinmann, *Helv. Phys. Acta.* **33** 257, 347 (1960); H. Epstein, in *Structural Analysis Of Collision Amplitudes* edited by R. Balian and D. Iagolnitzer (Amsterdam 1976), and references therein.
- [16] A. R. White, hep-ph/0002303 - *The Past and Future of S-Matrix Theory* in *Scattering*, edited by E. R. Pike and P. Sabatier (Academic Press, London) and references therein.
- [17] S. Coleman and B. Grossman, *Nucl. Phys.* **B203**, 205 (1982).